Integrative spatiotemporal map of nucleocytoplasmic transport

Barak Raveh[*,1,2,3,4], Roi Eliasian[1], Shaked Rashkovits[1], Daniel Russel[2,3,4], Ryo Hayama[5], Samuel E. Sparks[6], Digvijay Singh[7], Roderick Lim[9], Elizabeth Villa[7,8], Michael P. Rout[*,5], David Cowburn[*,6], Andrej Sali[*,2,3,4]

[1] School of Computer Science and Engineering, Hebrew University of Jerusalem, Jerusalem, Israel.

[2] Quantitative Biosciences Institute, University of California, San Francisco, San Francisco, CA 94158, USA.

[3] Department of Bioengineering and Therapeutic Sciences, University of California, San Francisco, San Francisco, CA 94158, USA.

[4] Department of Pharmaceutical Chemistry, University of California, San Francisco, San Francisco, CA 94158, USA

[5] Laboratory of Cellular and Structural Biology, The Rockefeller University, New York, NY 10065, USA

[6] Departments of Biochemistry and Systems & Computational Biology, Albert Einstein College of Medicine, Bronx, NY 10461, USA

[7] School of Biological Sciences, University of California San Diego, La Jolla, CA 92093, USA.

[8] Howard Hughes Medical Institute, University of California San Diego, La Jolla, CA 92093, USA.

[9] Biozentrum and the Swiss Nanoscience Institute, University of Basel, 4056 Basel, Switzerland.

*** Corresponding Authors**

Keywords: nucleocytoplasmic transport; nuclear pore complex; integrative modeling; spatiotemporal modeling; Brownian Dynamics simulations

Abstract

The Nuclear Pore Complex (NPC) facilitates rapid and selective nucleocytoplasmic transport of molecules as large as ribosomal subunits and viral capsids. It is not clear how key emergent properties of this transport arise from the system components and their interactions. To address this question, we constructed an integrative coarse-grained Brownian dynamics model of transport through a single NPC, followed by coupling it with a kinetic model of Ran-dependent transport in an entire cell. The microscopic model parameters were fitted to reflect experimental data and theoretical information regarding the transport, without making any assumptions about its emergent properties. The resulting reductionist model is validated by reproducing several features of transport not used for its construction, such as the morphology of the central transporter, rates of passive and facilitated diffusion as a function of size and valency, *in situ* radial distributions of pre-ribosomal subunits, and active transport rates for viral capsids. The model suggests that the NPC functions essentially as a virtual gate whose flexible phenylalanine-glycine (FG) repeat proteins raise an entropy barrier to diffusion through the pore. Importantly, this core functionality is greatly enhanced by several key design features, including 'fuzzy' and transient interactions, multivalency, redundancy in the copy number of FG nucleoporins, exponential coupling of transport kinetics and thermodynamics in accordance with the transition state theory, and coupling to the energy-reliant RanGTP concentration gradient. These design features result in the robust and resilient rate and selectivity of transport for a wide array of cargo ranging from a few kilodaltons to megadaltons in size. By dissecting these features, our model provides a quantitative starting point for rationally modulating the transport system and its artificial mimics.

The NPC. The Nuclear Pore Complex (NPC), a large protein assembly spanning the Nuclear Envelope (NE)[1–3], mediates selective macromolecular traffic between the nucleus and cytoplasm of the eukaryotic cell, a process known as nucleocytoplasmic transport. The NPC is composed of (i) a ring-shaped scaffold consisting of hundreds of protein subunits (nucleoporins or Nups) and (ii) the central transporter consisting of dozens of disordered phenylalanyl-glycyl (FG) rich repeat domains of FG Nups. The FG repeats are anchored inside the scaffold ring, thus occupying its central channel[4] (**Fig. 1a**). They play a major role in transport by forming a size-dependent barrier to passive diffusion, allowing passive translocation of ions, metabolites, and proteins smaller than a few dozen kDa while inhibiting the passage of larger macromolecules[5–7]. Larger macromolecular cargoes can nonetheless overcome this barrier and go through receptor-mediated facilitated diffusion, forming a molecular complex with nuclear transport receptors (NTRs) that interact directly with the FG repeats[8]. These cargoes include megadalton pre-ribosomal subunits, ribonucleoprotein (RNP) complexes, and even viral particles[9–13]. Given the large number and variety of cargoes, the NPC is involved in many cellular processes, such as gene regulation[14–17], genome organization[14], mRNA quality control[18], the cell cycle[19], and signal transduction[20]. Thus, NPC aberrations are associated with a number of disease states, disrupting vital cellular activities and potentially leading to pathologies such as cancer onset[21], viral infection[22], and neurodegenerative diseases[23–25].

Complexity of transport. Nucleocytoplasmic transport is complex because the transport system consists of many varied components whose interactions result in long cargo transit times on the time scale of milliseconds[26]. NPC proteins, featuring a mixture of structured and unstructured domains, interact both directly and indirectly with many dozens of other cellular proteins, RNAs, and RNPs[4,27–30]. Moreover, transport must be robust and resilient because it occurs in a noisy environment (*eg*, fluctuations in the NE shape, the NPC scaffold composition and geometry, energy availability, and cargo concentrations)[31–33]. Because the NPC operates over such a large range of spatial and temporal scales, no single experimental method can result in a model that is sufficiently accurate, precise, complete, and explanatory to study transport through the NPC at all relevant spatial and temporal scales[34] (**Fig. 1b**). Moreover, the inherent complexities of both the transport system and the experimental methods give rise to conflicting, noisy, and ambiguous measurements of the system and its components[35].

Prior models and challenges. As a result of this complexity, the mechanism underlying both passive and receptor-mediated facilitated diffusion is the subject of a lively scientific debate[2,5,7,36–56]. The transport system and its parts were modeled by us and others using varying representations, scales, and levels of granularity, including structural modeling of individual proteins at atomic resolution[57–59], atomistic or coarse-grained simulations of individual components such as FG repeats and NTRs[50,60], structural modeling of the whole NPC[4,28,29,61–64], spatiotemporal simulations of NPC dynamics or transport at varying resolutions[2,6,7,45,46,55,65–67], mathematical modeling of transport through individual NPCs[68,69], and mathematical modeling of transport at the cell level[70–72]. Different explanations have been suggested regarding the dependence of transport on sequence, charge, hydrophobicity, and cohesiveness of the FG

repeats[36,39,42,46,49,73,74]; the multi-valency, copy number per cargo, concentration, and spatial distribution of the NTRs[26,56,75–77]; the cargo size[5–7,75,78]; the RanGTP gradient across the NE[70,71]; the flexibility of the NPC scaffold[32,65,66,79,80]; and the NPC's response to mechanical stress[33,81]. A satisfactory transport model must explain existing data in terms of the transport system components and their interactions as well as provide testable quantitative predictions.

Addressing modeling challenges. Accurate, precise, complete, and explanatory modeling of transport is likely to be facilitated by using experimental and theoretical information across multiple spatial and temporal scales, while accounting for its sparseness, uncertainty, and ambiguity. Integrative modeling is a general approach that attempts to do so[35,82–86]. It has been successfully applied in structural biology to compute structural models of large macromolecular assemblies that are refractive to traditional single methods, including the NPC[4,28,29,83]. To expand the applicability of integrative modeling to even more complex and multi-scale systems, such as an entire cell, we recently developed Bayesian metamodeling[87]. Bayesian metamodeling is an instance of integrative modeling that aims to integrate varied input models (*eg*, a set of spatiotemporal molecular trajectories and a kinetic model specified by a set of ordinary differential equations) into a metamodel consisting of updated and harmonized input models[87].

Here, we used integrative modeling to compute spatiotemporal trajectories of molecules diffusing through a single NPC (**Fig. 1**), followed by Bayesian metamodeling to couple and harmonize these trajectories with our recent kinetic model of Ran-dependent transport in an entire cell[72]. Importantly, our model is reductionist in the sense that nucleocytoplasmic transport arises from the composition of the system and microscopic interactions between its components; thus, the model avoids phenomenological assumptions about key properties of the NPC, such as the saturated hydrogel and polymer brush properties of the FG repeats in the hydrogel[42] and virtual gating models[36], respectively. The composition and interactions in the model were parameterized to fit a large variety of experimental data and theoretical information across a broad range of spatial and temporal values (**Extended Data Table 1**). The resulting depiction was validated by its consistency with a number of observations that were not used in modeling. Next, the model was utilized to map the spatial and temporal features of nucleocytoplasmic transport as a function of the system components and their interactions (**Fig. 2-8**). Our model provides a number of explanations about key features of the NPC transport in terms of the system components and their interactions. In particular, we explain the biophysical origins of central transporter morphology (**Fig. 2**), how the NPC forms a size-dependent barrier to passively diffusing molecules (**Fig. 3**), how the microscopic details and the valency of the FG:NTR interactions facilitate the rapid diffusion of much larger cargoes (**Fig. 4-6**), how the coupling of facilitated diffusion to the RanGTP gradient further contributes to active transport of these large cargoes (**Fig. 7**), and how the geometry and composition of the NPC itself influence transport (**Fig. 8**). These results allowed us to conclude with a discussion of the molecular mechanism of transport.

Integrative spatiotemporal modeling of transport through the NPC

We first studied passive and facilitated diffusion of macromolecular cargo through a single NPC, initially without taking into account the RanGTP cycle (RanGTP-independent transport)[2,3,38,71]. This simplification is justified because RanGTP is not required for modulating the permeability of the NPC to NTR:cargo complexes[88]; for example, NTRs can facilitate equilibration across the NE independently from RanGTP[89].

We used integrative, data-driven coarse-grained Brownian dynamics simulations (**Fig. 1a; Supplementary Video 1**). The integration of multiple types of information allowed us to coarse-grain both the representation of the system and its trajectories, resulting in increased accuracy and efficiency of modeling. The modeling process consisted of the following four steps (**Methods**). First, we gathered varied experimental and theoretical information on the structure and dynamics of the transport system and its various components (**Fig. 1b, Extended Data Table 1**). Second, we created a coarse-grained Brownian dynamics representation of the transport system (**Fig. 1a**). Third, we computed a set of transport trajectories for each of the many combinations of parameter values (*eg*, interactions and diffusion constants), followed by systematically filtering these sets based on their fit to input information (*eg*, **Fig. 1c,d**, blue). Finally, we validated each filtered set of trajectories by quantifying how well it reproduces experimental data not used in its construction or filtering (*eg*, **Fig. 1c-e**). We describe each one of these steps in more detail next.

Step 1: Gather input information

In Step 1, input information was derived from multiple experimental and computational methods, providing extensive characterizations of the structure, dynamics, and thermodynamics of the entire yeast NPC (**Fig. 1b**; **Extended Data Table 1**). These characterizations included published datasets[4,34,39,50,90] as well as small-angle X-ray scattering (SAXS) profiles of FG Nups and atomistic molecular dynamics simulations of Kap95 in the presence of FSFG and GLFG repeats. We also relied on additional data for model validation, including published datasets[6,7,74,75,91,92] as well as an *in situ* cryo-electron tomography (cryo-ET) map of the central transporter and atomic force microscopy (AFM) images[93]. The scaffold model, including the localization of the FG Nup anchor domains, was provided by the complete integrative structure model of the yeast NPC[4]. This model is the starting point for the representation of transport (Step 2), computing and filtering of simulation trajectories (Step 3), and validation of the transport model (Step 4). To address the apparent inconsistencies between some datasets, such as those on the FG:FG interactions[36,39,42,49], we modeled transport for a range of parameter values (Steps 2-4) instead of including these datasets into model construction.

Step 2: Represent nucleocytoplasmic transport

The NPC and its environment are a dynamic system of interacting components (**Fig. 1a**). Model components include the NE, the scaffold of the yeast NPC embedded in the NE, the attachment sites of FG repeats to the scaffold, the dynamics of these FG repeats, NTR:cargo complexes

with multiple interaction sites for FG repeats, and passively diffusing individual macromolecules that do not interact specifically with FG repeats. Each nucleoporin domain was represented by up to a few spherical beads, totalling 20,272 beads per NPC for the disordered FG repeats alone. Interactions among these components and with their environment were parameterized based on input information, including prior work. To efficiently model the transport trajectories, we relied on the Brownian dynamics scheme[94]. Brownian dynamics simulations have been previously shown to provide useful dynamic depictions of protein-protein interactions[95], including in the crowded environment of the cell[96] and the NPC[4,7,45].

Step 3: Compute and filter transport trajectory sets

We proceeded in two stages to reduce computational cost (**Methods**). First, many combinations of uncertain model design features (*eg*, model granularity and interaction parameter values) were filtered to retain only those model instances that produced trajectories consistent with the experimental data, resulting in an improved fit of the model to a subset of the data. Second, extensive production trajectories were generated using the tuned model.

Brownian dynamics simulations were implemented in our open-source *Integrative Modeling Platform* software (www.integrativemodeling.org)[4,7]. A starting configuration is propagated in ~10^8 small steps, reflecting the interactions between the components and small random forces, resulting in a ~0.1 ms trajectory. Because transport is a relatively rapid but rare stochastic event[26,97], thousands of independent trajectories starting from random configurations were computed for each set of conditions, leading to an aggregate simulation time of several seconds.

To compute both the filtering and production trajectories, we had to use extensive computational resources. The filtering stage produced millions of relatively short trajectories (5-10 μs) on Google Exacycle, benefiting from frequent overnight runs on several hundred thousand CPUs, and on thousands of CPUs on our own Linux high-performance computing cluster at UCSF. The subsequent production trajectories required a few million CPU core hours on our cluster.

Step 4: Validate the model

The model is validated in four ways, as follows. First, we estimate model uncertainty (precision) corresponding to the variation among a set of independent trajectories. These uncertainties were quantified by the confidence intervals for model properties, such as density maps and transport rates, estimated from the trajectories[98]. Thus, we first verify that the cumulative simulation time resulted in sufficiently precise estimates to justify our conclusions. Second, we ensure that the model, including its representation and parameter values, is consistent with information used and not used to construct it. This goal is achieved by using some data for defining model representation and filtering transport trajectories as well as other data for validating the filtered trajectories. Third, we compensate for the remaining uncertainty about model representation and parameter values by interpreting the trajectories computed for a range of uncertain parameter values. Finally, we use our model to rationalize available

experimental and theoretical information, to make new testable predictions, and to provide explanations about the modeled system. In seeking mechanistic insight into the nucleocytoplasmic transport, we benefit from the reductionist nature of the model that maps the system behavior in terms of its components and interactions between them.

The model reproduces key biochemical characterizations of multivalent FG:NTR interactions not used during model construction

Given the established role of FG repeat – NTR:cargo interactions, we first ensured that our model accurately represents these essential components. Specifically, we assessed whether the simulated FG repeats and NTR:cargo complexes reproduce key biochemical measurements, including those not utilized for model construction. The FG repeats were parameterized to match the known radius of gyration, end-to-end distance, and relaxation time (**Extended Data Table 1**). Additionally, the interaction between a single FG motif and an NTR molecule (NTF2) was parameterized to reproduce the corresponding dissociation constant, measured by NMR titrations and Isothermal Titration Calorimetry (ITC) (**Fig. 1d**, blue**; Extended Data Table 1**)[90]. To validate the model using data not used for model construction, we compared the simulated and measured avidity data for multivalent FG repeat constructs with 2, 3, 4, or 6 FG motifs (**Fig. 1c-e**). The model reproduced not only the dissociation constants computed from NMR and ITC experiments (**Fig. 1e**), but also the raw NMR titration data quantifying the fraction of bound chains for a wide range of FG valencies and concentrations (**Fig. 1d**). In fact, the difference between the model and NMR data was smaller than that between the NMR and ITC measurements (**Fig. 1e**), despite a non-linear relation between the FG valencies and their NTR avidities, which cannot be explained by simple kinetic modeling[90]. The accurate prediction of this non-linear empirical relation highlights a contribution of an explicit spatiotemporal representation compared to a more abstract representation used in kinetic modeling. In conclusion, the independent validation of the model by NMR and ITC data indicates that it accurately represents the interactions between its key components, thus increasing our confidence in other model predictions.

The model reproduces rapid exchange of interacting FG repeats and NTRs through anisotropic sliding

FG repeats and NTRs exchange at an unusually rapid rate compared to other proteins interacting with similar affinity[47,48]. This rapid exchange is explained by a 'fuzzy' slide-and-exchange interaction[34,50], based on long molecular dynamics simulations and supporting NMR experiments. According to this mechanism, FG motifs slide along NTR binding grooves, analogously to the sliding of transcription factors as they rapidly locate their binding sites on DNA[99]. However, sliding has been demonstrated for only one NTR (NTF2) interacting with one flavor of FG repeats (FSFGs)[50]. To establish whether sliding occurs between other types of NTRs and FG repeats, we performed atomistic molecular dynamics simulations[100] of FG repeats in the presence of karyopherin Kap95 (importin subunit β-1)[101]. Despite the

significant structural differences between Kap95 and NTF2, the simulations show that the FG motifs also slide through the grooves between adjacent Kap95 helices (**Supplementary Video 2**), as visualized by a principal component analysis of the FSFG motif center-of-mass sliding on Kap95 (**Fig. 1f**; **Supplementary Video 3**). Thus, the slide-and-exchange mechanism is substantiated by molecular dynamics simulations of both major families of NTRs that interact directly with the NPC[59,102–104].

Next, we evaluated whether sliding can indeed contribute to the exchange rate of FG repeats on NTRs at physiological concentrations, as previously hypothesized[50]. To do so, we assessed two alternative forms of the interaction between FG repeats and NTRs in our coarse-grained model, resulting in a sliding and non-sliding interaction mode, respectively (**Fig. 1g**). For the sliding mode, FG repeats interact with NTRs anisotropically, as observed in the atomistic molecular dynamics simulations[50]. For the non-sliding mode, the interaction is isotropic, depending only on the distance, but not on the relative orientation of the FG motif and its interaction site. In both modes, interaction parameters were optimized to reproduce the empirical interaction affinity for a single FG motif interacting with a single NTR **(Fig. 1g**, left). As predicted by the atomistic molecular dynamics simulations, sliding of competing FG motifs also facilitates faster exchange in the coarse-grained Brownian dynamics simulations; the simulated on- and off-rates (**Fig. 1g**, middle and right, respectively) are an order of magnitude higher for the sliding than non-sliding mode. The accurate reproduction of the rapid exchange between FG repeats and NTRs[47,48] in the context of multivalent interactions[90] justifies using the sliding mode in our coarse-grained model. The effect of sliding on facilitated diffusion is discussed below.

The model reproduces the effect of anchoring FG repeats on their polymer properties

We proceeded by comparing polymer properties of the anchored FG repeats in the central transporter and freely-diffusing FG repeats in a buffer. Recent *in situ* FRET measurements indicated that the FG repeats of hNup98, the human ortholog of Nup100, are significantly more extended in the NPC than in a dilute buffer[74]. Because these data were not available during model construction, we can use them to test how well the model describes the effect of the NPC milieu on the FG repeats. Although the model was trained to reproduce the relatively low end-to-end distance (R_E) of Nup100 measured in buffer (**Extended Data Figs. 1-2; Supplementary Data Tables 2-3**), it recapitulated the empirical increase in R_E in the NPC, caused by the anchoring of the multiple FG Nups to the NPC scaffold: For a Nup100 FG repeat segment of 260 residues, the simulated R_E increased from 82 ± 1 Å in the dilute buffer to 124 ± 1 Å in the NPC; in the experiment, it increased from 74 Å to 130 Å[74] (**Extended Data Fig. 2b**). Thus, the model correctly describes how the context of the NPC scaffold modifies the intrinsic polymer properties of FG repeats, in agreement with the suggested transitioning from a poor-solvent to the theta-solvent regime *in situ*[74,105].

The model reproduces salient morphological features of the central transporter

We next address the morphology of the central transporter (**Fig. 2**). We begin by testing how well the model reproduces the density distribution of FG repeats, NTRs, and cargo molecules in the central channel of the NPC (*ie*, the central transporter)[4,77,93]. Originally termed the central plug[106], the central transporter has been often omitted from electron microscopy (EM) reconstructions of the NPC, due to the heterogeneity of its composition and structure[61,64,107]. Nevertheless, the averaged cryo-ET subtomogram map of the isolated yeast NPC[4] revealed three interrelated features of the central transporter (**Fig. 2a**), namely (i) a “moat” of low density surrounding the high-density region at the center of the central channel, (ii) “thin connections" of higher density that radially traverse the moat, and (iii) a central high-density region connected to the NPC scaffold *via* the thin connections. To compare our model and the EM maps of the central transporter, we averaged the densities of the FG repeats and NTRs in the ensemble of transport trajectories (**Fig. 2b**); in addition, the computed density not originally symmetrically averaged was also averaged using C_8 symmetry, as for the experimental maps. The resulting simulated density map recapitulates the moat, thin connections, and the high-density region near the central axis in the cryo-ET map (**Fig. 2a,b,** insets), even though these features were not included in modeling.

For further validation, we also compared our model with a new *in situ* cryo-ET map (**Fig. 2a; Extended Data Fig. 3)**. While the resolution of the *in situ* cryo-ET map is lower than that of the *in vitro* cryo-ET map (44 *vs* 28 Å), the *in situ* map is also consistent with the moat, thin connections, and central high-density features in our model. These similarities among the *in vitro* and *in situ* cryo-ET maps as well as model densities of the central transporter further increase our confidence in the model’s applicability to functional NPCs. Thin connections surrounded by a low-density moat are also clearly evident in other recent *in situ* cryo-ET and single particle isolated NPC maps of the central transporter[62,108].

Next, we interpreted the cryo-ET maps with the aid of the ensemble of transport trajectories. It may be tempting to explain the low-density moat as a peripheral cavity and the high-density thin connections as stable ultrastructures that protrude from the scaffold walls towards the central axis of the NPC. However, neither the moat nor thin connections appear in any one simulation snapshot (**Fig. 2c**), only in the density map for the entire ensemble of trajectories (**Fig. 2b**). Thus, our model indicates that the moat and thin connections in the cryo-ET maps should be interpreted respectively as low- and high-occupancy regions in a broadly distributed ensemble of disordered FG repeats, resulting from C_8 averaging of thousands of NPC particles in cryo-ET map construction. As for the central high-density region, the model suggests that it consists of both FG repeats and NTRs plus cargoes; the density of FG repeats is higher at the periphery than near the central axis, while the opposite is the case for the NTRs (**Fig. 2b**, bottom).

Thin connections are formed due to entropic confinement of FG repeats near the scaffold walls

Because the moat and thin connections arise from the interactions between the model components over time, an analysis of simulated trajectories allows us to describe how they form. We hypothesized that the high-density thin connections emerge due to the entropic confinement of the flexible FG repeats away from the NPC scaffold[36,62,109]. A theoretical underpinning for this observation is provided by a smaller number of configurations of a flexible polymer close to its anchor point compared to a non-confined state closer to the center of the transporter (**Fig. 2d**). To test this hypothesis in a simpler setting, we simulated flexible polymers anchored to the walls of a cylinder, similarly to our previous miniature model of the NPC[7]. As expected, for a broad range of model parameter values, the simulations resulted in the C_8 floret pattern seen in the actual central transporter, with low-density regions close to the FG repeat anchor points (**Fig. 2e**). The C_8 floret pattern is also visible in previously published simulations in which FG repeats were represented as disordered polypeptides anchored to a fixed cylinder, although the pattern was not discussed[2,110]. Thus, the entropy confinement is indeed a plausible rationalization of the thin connections in terms of the interactions between the system components, validating the model beyond the simple observation of the fits to the cryo-ET maps.

Densities of actively and passively diffusing molecules at the central transporter are distinct but overlapping

The model indicates that the cargo:NTR density is shifted towards the central axis of the NPC relative to the density of the FG repeats (**Fig. 2b**), with two high-density “lobes" along the channel axis forming at the cytoplasmic and nuclear sides of the central transporter (**Fig. 2g**, red). The lobes are consistent with high-density regions in the *in vitro* cryo-ET map (**Fig. 2f**, gray). We thus interpret the high-density lobes in the cryo-ET map to result from the high-occupancy of the NTR:cargo complexes, in agreement with the large fraction of cargo molecules and NTRs found in a mass spectrometry analysis of NPCs[4]. The distribution of both cargo:NTR complexes and FG repeats is nonetheless broad, with lower densities observed well into the cytoplasm and nucleus (**Fig. 2g**), consistent with the cryo-ET map[4] and recent super-resolution 3D imaging of translocating cargo molecules[26].

The density of passively diffusing molecules is shifted even further towards the central axis of the central transporter compared with that of the cargo:NTR complexes (**Fig. 2h,i**), in agreement with imaging of the radial preference for passive diffusion[111,112]. As expected, the absolute density of the NTR:cargo complexes is much higher than that of passively diffusing molecules (**Fig. 2i, top**). In relative terms, the NTR:cargo complex density is shifted towards the FG densities, peaking midway between the central axis and scaffold walls (**Fig. 2i**). The partial overlap between the cargo:NTR and FG densities (**Fig. 2g,i**) arises from a balance between their attractive interactions and repulsive excluded volume effect.

The model reproduces size-dependent fluxes for passive diffusion

We next test predictions of the flux of passively diffusing molecules against the experiment. In the model, the rate of diffusion is measured along the reaction coordinate corresponding to the NPC central axis, bounded by the two sides of the central transporter channel. The rate corresponds to the NPC permeability (p), an intrinsic property of the NPC for a given diffusing molecule[5,7,78]; p is estimated from simulation by counting the number of diffusing molecules that pass through the NPC reaching the opposite channel opening per unit of time per unit of the difference in the concentrations of the diffusing molecules in the cytoplasmic and nuclear compartments (ΔC); the flux through a single NPC is $p\,\Delta C$, according to the Fick's first law. The permeability of the NPC in the model decreased gradually as a cubic root of the molecular weight of the diffusing molecule (**Fig. 3a**) (or, equivalently, as an exponent of its molecular radius with a decay constant of -0.37 $Å^{-1}$; **Extended data Fig. 4a**). This result is in agreement with both our *in vivo* FRAP measurements of transport rates and previous simulations of a simpler model of the NPC consisting of a cylindrical pore lined with generic flexible polymers (**Fig. 3a**)[7]. It also fits experimental results for passively diffusing molecules of varying sizes, shapes, and domain compositions[6,7]. These agreements indicate that a flexible polymer anchored to the scaffold walls is sufficient to provide a size-dependent barrier to passive diffusion[36,109]. Both the model and *in vivo* experimental data indicate that passive diffusion diminishes continuously with increasing molecular weight rather than having a well-defined size threshold (*eg*, 30-60 kDa), in agreement with our previous studies of passive diffusion[7].

NPC permeability to passive diffusion is conserved across multiple species

We examined whether or not the size-dependence of passive diffusion in yeast is conserved in other organisms and cell types. For example, a *Xenopus* oocyte is a highly specialized cell with a diameter that is 200-300 times larger than that of the yeast cell[7,11,113], resulting in a seven orders of magnitude larger volume. Moreover, the half-life for the decrease in the difference between the concentrations of the passively diffusing molecules in the cytoplasm and nucleus (*ie*, the equilibration time) is two orders of magnitude longer than in yeast[11,114,115]. Nevertheless, this observation is rationalized simply by Fick's first law[7], based on the volumes of the cytoplasm and nucleus[11,114] as well as parsimoniously assuming the same NPC surface density in both organisms; in particular, the yeast simulations accurately predict the transport rates for dextrans and ovalbumin in *Xenopus* oocytes (**Fig. 3a**). Thus, the permeability of a single NPC to passively diffusing molecules appears to be highly conserved across species. A similar calculation for other cell types indicates that *in vivo* equilibration times in most cells are slower but still on the same order of magnitude as in yeast (**Extended Data Fig. 2b**). Thus, our NPC model may accurately quantify NPC transport rates across multiple species, not only yeast. This generality increases our confidence in the nucleocytoplasmic transport mechanism suggested by the model.

Relation between fluxes and densities is rationalized by the transition state theory

We assessed whether the changes in the flux of passively diffusing molecules as a function of their size correspond to changes in their density inside the NPC. The model shows that the density of passively diffusing molecules is indeed lower inside than outside of the NPC, with the decrease being more pronounced for larger, low-flux molecules (**Fig. 3b-e**). The dependence of the flux on the density in our model is rationalized with the aid of the Eyring-Polanyi equation embodying the transition state theory (TST)[116,117], as follows. In TST, an elementary chemical reaction proceeds from reactants to products through a transition state. The Eyring-Polanyi equation predicts that the reaction rate decreases exponentially as a function of the Gibbs free energy difference between the ground and transition states (free energy barrier). It has been argued based on theoretical grounds that TST also applies to diffusion in a narrow pore without polymer brushes[118]. Thus, in the NPC, the reaction coordinate is the central axis of the channel, the reactants are molecules on one side of the NPC, the products are the same molecules on the other side of the NPC, and the transition state corresponds to populating the central transporter of the NPC. This proposed equivalence was previously confirmed in simulations of diffusion through homogeneous polymer brushes arranged in even layers in a cylindrical channel[2,7,91].

Our spatiotemporal model allows us to assess whether the Eyring-Polanyi equation holds for the unabridged NPC geometry, FG Nup anchoring patterns, and FG Nup composition. The free energy barrier was estimated *via* the Boltzmann inversion of the observed steady-state density of diffusing molecules. The resulting 2D and 1D free energy maps show that the free energy barrier for passive diffusion increases linearly with molecular radius and approximately linearly with molecular weight (**Fig. 3b-e; Extended Data Fig. 4c**)[7,111], by 1 kT for every 0.5 nm in radius and 34 kDa in molecular weight, respectively. In a remarkable agreement with TST, permeability to passive diffusion indeed depends exponentially on the free energy barrier of transport (**Fig. 3f**), fitting the Eyring-Polanyi equation with R^2=0.999. This result is consistent with the slow exponential decay of NPC permeability as a function of the diffusing molecule radius (**Extended Data Fig. 2a**) and its cubic decay as a function of the diffusing molecule molecular weight (**Fig. 3a**), observed in both simulation and experiment. Thus, the kinetics of passive diffusion may be modeled as that of an elementary chemical reaction, even for the NPC. Finally, the direct correspondence between the free energy barrier and the kinetics of passive transport indicates that the steady-state densities of passively diffusing molecules highlight spatial pathways for passive diffusion.

The density of NTR:cargo complexes decreases slowly with molecular weight

We next investigated how NTRs mediate rapid facilitated diffusion for much larger cargo molecules. We begin by relating the density, flux, and size of NTR:cargo complexes, once again employing the TST. We assessed how the densities of the NTR:cargo complexes change as

their molecular weight increases from 14 kDa to 133 kDa (**Fig. 4**); in this analysis, we used a fixed NTR valency of 4 sites, where NTR valency is defined as the number of interaction sites for FG repeats on each NTR. Compared with passively diffusing molecules, the densities of the NTR:cargo complexes inside the central channel decreased much more slowly as a function of their molecular weight (**Fig. 4a,b**). Moreover, despite the weak (millimolar) affinities of individual interaction sites (**Fig. 1c,d,e**), the concentrations of the NTR:cargo complexes were much higher than those of passively diffusing molecules of the same molecular weight (**Fig. 4b**). The high densities of the NTR:cargo complexes are explained by the avidity (higher affinity) of NTRs with multiple interaction sites (**Fig. 1d,e,g**)[119]. These densities are consistent with the bright NPC-associated staining of many NTR:cargo complexes seen in actual cells[76], the relatively large total mass of the NTR:cargo complexes (>26 MDa) in the yeast NPC[4], and the 20-50 mM concentration of individual FG motifs in the central channel[4,42,54], which is higher than the measured dissociation constant for NTRs (**Fig. 1e**)[90].

The high density of large NTR:cargo complexes reflects rapid transport fluxes

The higher densities of NTR:cargo complexes imply that the simulated free energy barrier for facilitated diffusion is lower than that for the passively diffusing molecules (**Fig. 4c,d**). In fact, the free energy for facilitated diffusion has a local minimum in the central channel on either side of the maximum at its equator (Z=0 nm). This free energy barrier was only modestly higher for large than for small molecules (**Fig. 4d**). As expected, the much higher densities and lower free energy barriers of the NTR:cargo complexes compared to passively diffusing molecules were indeed manifested in higher permeability for facilitated than passive diffusion. Nonetheless, NTRs with larger cargo molecules were distributed farther from the NPC "equator" at Z=0 (**Fig. 2e**) and closer to the central axis of the NPC compared to NTRs with smaller cargo molecules (**Fig. 2f**), again in agreement with previous observations[111]. This size-dependent difference is rationalized by the higher density of FG repeats away from the central axis, which exerts a stronger repulsive force on larger cargo molecules, pushing them towards the less dense regions.

The size-dependence of facilitated diffusion is reproduced by the model

While passive diffusion rates decrease rapidly with molecular weight (~MW^{-3}), facilitated diffusion of NTR:cargo complexes has a significantly weaker dependence on molecular weight (~$MW^{-2/3}$) (**Fig. 4g**), as expected from *in vivo* measurements of size-dependent facilitated diffusion in mouse embryonic fibroblasts[72]. The NPC selectivity, defined as its permeability to facilitated diffusion of a given cargo divided by its permeability to passive diffusion of the same cargo, increases from 30-fold for 14 kDa molecules to 1000-fold for 133 kDa molecules. As a result, the facilitated diffusion rate of a 133 kDa NTR:cargo complex is predicted to be 50% faster than that of a 14 kDa molecule, whereas its passive diffusion rate is 1000-fold slower, in agreement with experiment[7]. Moreover, the model reproduces experimental results showing that even small cargo molecules (~20 kDa) are transported significantly faster *via* facilitated diffusion than passive diffusion[5], thus rationalizing why even relatively small cargo molecules may require

an NTR for their import into the nucleus (*eg*, Ran requires NTF2)[5,102]. Thus, our spatiotemporal model recapitulates the speed, size-dependency, and weak size-dependence of facilitated transport[5].

Slide-and-exchange increases the rate of facilitated diffusion by an order of magnitude

We used our model to investigate how interactions between NTR:cargo complexes and FG repeats impact the kinetics of facilitated diffusion, all else being equal. We have already established that slide-and-exchange of FG repeats on NTF2[50] and karyopherins (**Fig. 1f**) results in a rapid molecular exchange, in agreement with experiment[47,48,50]. We hypothesized that slide-and-exchange contributes to reduction of resistance to the flow of the NTR:cargo complexes through the NPC. Flow resistance can be quantified by dynamic viscosity, which is inversely proportional to the diffusion coefficient according to the Einstein-Stokes relation[120,121]. With sliding, the apparent diffusion coefficient of the NTR:cargo complexes within the central channel is indeed only 32 - 43% slower than in the cytoplasm, compared to a 44 - 66% reduction without sliding, in agreement with previous experimental estimates of the NTF2 diffusion coefficient within the central transporter[5] (**Fig. 4h**). Thus, slide-and-exchange helps compensate for added molecular crowding in the pore, resulting in almost no change in dynamic viscosity for diffusing cargo:NTR complexes when they enter or exit the pore. Correspondingly, the permeability of the NPC to NTR:cargo complexes was 1-2 orders of magnitude higher with sliding of NTR:cargo complexes than without sliding (**Fig. 4i**, red *vs* pink), everything else, including NTR:FG repeat avidities, being equal (**Fig. 1g**, left). Furthermore, sliding contributed to size-dependence by disproportionally increasing the permeability of the NPC to larger NTR:cargo complexes (**Fig. 4i**, pink *vs* blue). Without sliding, facilitated diffusion of these larger complexes was nearly as slow as passive diffusion. Thus, slide-and-exchange is predicted to contribute significantly to both the speed and selectivity of nucleocytoplasmic transport.

The number of FG interaction sites on NTRs modulates facilitated diffusion rates

We next characterize how the multivalency of NTR:cargo complexes influences facilitated diffusion kinetics, revealing a tradeoff between valency and cargo size. Various NTRs, including larger ones such as Kap95[122] and CRM1[58], and the comparatively smaller ones such as NTF2[57], have multiple interaction sites for FG repeats[122,123]. In addition, some cargo molecules interact with multiple NTRs simultaneously, resulting in an NTR:cargo complex of overall higher valency[59]. This valency impacts the avidity and exchange rates[124–126] between FG repeats and NTRs[90,127], but its effect on the kinetics of facilitated diffusion has not yet been comprehensively quantified, though several studies have indicated that adding a small number of NTRs to a cargo molecule can result in faster transport[75,97].

We compared trajectories of NTR:cargo complexes with identical molecular weights, but with the number of FG interaction sites varying from zero to eight (**Fig. 5**). As expected, their central transporter densities increase over the entire range; the density of complexes with even a single

interaction site is already six-fold higher relative to complexes with no interaction sites (*ie*, equivalent to passive diffusion). For four sites or more, the central channel contains more NTRs than the cytoplasmic and nuclear peripheries (**Fig. 5a,b**); correspondingly, the free energy within the central transporter is lower than in the NPC periphery (**Fig. 5c,d**).

The gradual decrease in the free energy barrier due to the addition of FG interaction sites on an NTR results in an exponential increase in the permeability of the NPC for facilitated diffusion (**Fig. 5e**). Even a single interaction site is sufficient for a modest but notable three-fold increase in the NPC permeability (**Fig. 5e**), while six interaction sites increase the permeability by almost three orders of magnitude. However, as the number of sites increases further from six to eight, permeability begins to decrease, likely reflecting a tradeoff between the decrease in the free energy barrier of passive diffusion and entrapment within the central channel, resulting in decreased diffusion. In conclusion, our spatiotemporal reductionist model quantitatively reproduces, and thus rationalizes, how the rate of facilitated diffusion changes as a function of the number of FG interaction sites on the NTR.

A tradeoff between the NTR valency and cargo size results in efficient facilitated diffusion of very large cargo

We performed simulations in which we varied both the number of FG binding sites on the NTR surface from 0 to 16 and the size of the NTR:cargo complex from 16 kDa to 1.4 MDa. In total, 70 combinations of cargo size and valency were simulated for 80 μs each. Each simulation was repeated 100 times, for a total of 7,000 trajectories covering 500 seconds of facilitated diffusion.

For smaller NTR:cargo complexes (<400 kDa), the permeability increases exponentially as a function of NTR valency, from 0 to 6 FG interaction sites (**Fig. 6a**). For larger complexes (>400 kDa), significant facilitated diffusion is not observed for 0 to 4 sites, while it does occur for 6 or more interaction sites. However, permeabilities of the smaller complexes begin to decrease markedly for more than 6 sites, dropping to zero for 12 or more sites. In contrast, for larger complexes, the permeability decreases only slightly, or even increases, with additional interaction sites. As expected, for 0 interaction sites (*ie,* for passive diffusion), permeability sharply decreases with molecular weight, following the inverse cubic power law (**Fig. 6b**). As the number of sites increases to 6, the relatively high permeability decreases more gradually with molecular weight. For more than 6 sites, the diffusion does not depend on the cargo size, indicating that high valency benefits larger cargos more than smaller cargos. As a result, the significant decrease in the permeability due to molecular weight (**Fig. 3a**) can be counteracted by adding a relatively small number of sites (**Fig. 6a,b**). This observation is in line with experiment[75,97] and resolves the apparent contradiction between the ability of the NPC to translocate larger MDa cargo molecules while significantly slowing the passive diffusion of small <50 kDa macromolecules.

Our model indicates that several particles the size of pre-ribosomal subunits and viral capsids can occupy the central transporter simultaneously (**Fig. 6c**), despite the voids that they

introduce within the thicket of FG repeats (**Fig. 6d**). This result is validated by the recent cryo-EM structures of native pre-60S ribosomal particles within the NPC, showing multiple particles occupying the central transporter of the NPC with a relatively small number of accompanying NTRs[92]. Our model predicts that the multivalent interactions of the NTRs compensate for the entropic restriction of the FG repeats by these large particles. An additional strong validation of our model is provided by a comparison of the radial distribution of large particles in our simulations (diameter of 15 nm) and the recently measured radial distribution of the pre-60S particles (diameter of 21 nm) in the central channel[92] (**Fig. 6e**). Our model correctly predicts that transport pathways are broadly distributed with a peak approximately 10 nm from the central axis of the NPC.

Active Ran-dependent transport of large cargos is rationalized by coupling the spatiotemporal NPC transport model with a kinetic cell model

We next assessed our model of receptor-mediated facilitated diffusion of large cargoes in the context of experimental measurements in cells. Transport of large cargo molecules has been characterized experimentally in, among other systems, digitonin-permeabilized HeLa cells[75,97] as well as live starfish and Xenopus oocytes[75]. In cells, the NPC transport is energy-dependent and directional due to the concentration gradient of the RanGTP protein across the NE (active transport)[88,128]. This gradient provides the energy for directional transport through asymmetric dissociation of imported and exported complexes on the nuclear and cytoplasmic sides of the NPC, respectively[2,129,130]. In contrast, in our spatiotemporal model, transport is not energy-dependent nor directional, due to the absence of RanGTP. Therefore, the experiments quantify active Ran-dependent transport rates of cargo:NTR complexes under non-equilibrium conditions, whereas our spatiotemporal model quantifies non-active facilitated diffusion rates under equilibrium conditions.

Both the experimental measurements and simulations (**Figs. 5 and 6**) indicate that a relatively small number of nuclear localization sequences (NLSs) are sufficient to allow translocation of very large (> MDa) cargo molecules. This agreement is consistent with the finding that RanGTP hydrolysis is not directly coupled to any molecular rearrangement of the NPC[2]; indeed, reversing the RanGTP gradient leads to a reversal of transport direction[88]. Thus, Ran is not required for rationalizing how large cargo permeates the NPC.

However, our simulations (**Figs. 5e and 6a,b**) initially did not reproduce the monotonic increase in the transport rate with additional FG interaction sites[75] (**Fig. 7a**). We investigated this discrepancy by considering RanGTP-dependent transport in an entire cell and RanGTP-independent transport through a single NPC in the context of each other (**Fig. 7b**). To do so, we used our recent metamodeling approach[87]. In this approach, a complex biological system is represented by a set of coupled models of different aspects and/or parts of the system (*eg*, trajectories of protein molecules and a network of protein-protein interactions). The models are then updated with respect to each other to obtain a more accurate, precise, complete, and explanatory depiction of the system (a metamodel). Here, a metamodel of RanGTP-dependent

active transport in the cell couples two models. The first one is our spatiotemporal model of RanGTP-independent facilitated diffusion through a single NPC. The second model is our recent kinetic model of RanGTP-dependent transport in the cell[72]. The kinetic model aims to capture the broadly accepted canonical assumptions about RanGTP-dependent transport[2,53,70,71,131] using a system of ordinary differential equations whose rate constants were fit to empirical measurements[72]. It describes facilitated diffusion of NTR:cargo complexes, passive diffusion of unbound cargo molecules, the RanGTP-dependent release of cargo in the nucleus, and the energy-dependent cycle that replenishes the concentration gradient of RanGTP across the NE. The parameters include rate constants for docking of the NTR:cargo complexes to the NPC and the facilitated diffusion rate of the NTR:cargo complexes between the cytoplasmic and nuclear sides of a single NPC (**Fig. 7a,** third column). These kinetic model parameters are coupled with the corresponding spatiotemporal model parameters, allowing us to refine their values using the metamodeling approach[87]. The result is a metamodel of nucleocytoplasmic transport at both single NPC and cell levels.

The metamodel (**Fig. 7b**) resolves the above-mentioned discrepancy between the monotonic increase in measured RanGTP-dependent transport rates[75] (**Fig. 7a**) and the saturation of simulated RanGTP-independent permeabilities as a function of valency (**Figs. 5e and 6a,b**). The metamodel predicts correctly that the initial flux and nuclear concentration of cargo increase markedly and monotonically when the docking affinity of NTR:cargo complexes to the FG repeats increases, even if the NPC permeability remains constant (**Fig. 7c; Extended Data Fig. 5a**). To verify that this effect is due to the RanGTP concentration gradient, we used a negative control simulation in which RanGTP could not release NTR:cargo complexes. As expected, increasing the docking affinity beyond a threshold indeed results in a decrease in the rate of equilibration across the NE (**Fig. 7d; Extended Data Fig. 5b**). Moreover, given that the NPC-bound NTRs could no longer dissociate from the cargo *via* binding to RanGTP, cargo:NTR complexes accumulated within the NPC (**Extended Data Fig. 5b**, bottom row), in agreement with experimental disruption of RanGTP-mediated cargo release[76]. In conclusion, both the spatiotemporal model of a single NPC and the kinetic model of the cell are validated by the experimental observations (**Fig. 7a** *vs* **Fig. 7c**). Thus, they provide a rationalization of how higher avidity for the NPC increases transport rates under non-equilibrium (Ran-dependent) conditions, but not under equilibrium conditions (**Fig. 7c** *vs* **Fig. 7d**).

Interactions between FG motifs are not essential for fast and selective transport

We characterize how perturbations of the composition and geometry of the NPC influence the size-dependence and rates of facilitated and passive diffusion, and consequently, transport selectivity. We begin by assessing the impact of FG:FG interactions. Some phenomenological models of transport suggest that transport selectivity arises mostly from the interactions between pairs of FG motifs, based on experiments with saturated FG repeat hydrogels that by definition consist of highly cohesive FG repeats[42]. Alternatively, other phenomenological models

suggest that selectivity arises mostly from the entropic cost of restricting the FG repeat conformations[36,37].

To address whether or not FG:FG interactions are essential for fast and selective transport, we repeated coarse-grained Brownian dynamics simulations with either reduced or increased interactions between all types of FG motifs (including both FSFG-like and GLFG-like motifs). When FG:FG interactions are eliminated entirely, the permeability of the NPC for both facilitated and passive diffusion increases in comparison to the wildtype NPC (**Fig. 8a**, right panel, yellow *vs* green). However, even without any FG:FG interactions, passive diffusion remains size-dependent. As a result, the permeability for facilitated diffusion is orders of magnitude higher than for passive diffusion (**Fig. 8a-b**, yellow), albeit the transport selectivity of the wildtype is even stronger (**Fig. 8b**, green). Thus, interactions between pairs of FG motifs are not essential for a rapid and selective transport.

'Fuzzy' FG:FG interactions may contribute to robustness of selective transport

The permeability decreases with an increase in the strength of the FG:FG interactions among all or some types of FG motifs (**Fig. 8a**). However, it decreases more strongly for facilitated than for passive diffusion, reducing the selectivity relative to the native NPC (**Fig. 8b**, cyan). Thus, according to our model, overly strong FG:FG interactions may reduce transport selectivity altogether. In contrast, a moderate level of FG:FG interactions in the native NPC leading to short-lived and 'fuzzy' FG:FG interactions on the order of picosecond to nanosecond is consistent with the empirically-observed fast exchange of FG repeats and NTRs[47,48,50] (**Figs. 1g and 4i**). Thus, moderate FG:FG interactions can improve selectivity. They may also contribute to the robustness of transport by, for example, limiting undesired leakage through the NPC. Such moderate interactions are consistent with the radius of gyration of the FG repeats of some FG Nups, mainly GLFG repeats[39], which in our model are fitted to SAXS, SANS, and FPLC experimental data and atomistic molecular dynamic simulations (**Extended Data Fig. 2a**). The mild FG:FG interactions are also consistent with the previously discussed increase of the end-to-end distance of the GLFG-rich Nup100 *in situ* relative to buffer in both FRET experiments[74] and our model (**Extended Data Fig. 2b**), implying that FG:FG interactions are sufficiently weak to be overcome in the crowded environment of the central channel. Moderate FG:FG interactions are also consistent with the suggested mechanism for the robustness of the NPC to clogging[56], while still accounting for the reported higher-density regions in central channel[66]. A detailed characterization of the heterogeneity among FG:FG interactions in different types of FG Nups[132] remains beyond the scope of the current work.

NTRs provide resiliency against loss of FG:FG interactions

To test our predictions regarding the influence of FG:FG interactions on transport, we compared them to previous experiments and simulations of transport in artificial nanopores grafted with FG repeat domains of either Nsp1 or Nsp1-S[91]. Nsp1-S is identical to Nsp1 except for the hydrophobic FG residues that are mutated to the hydrophilic SG residues. These mutations are

expected to have two major consequences: First, by reducing hydrophobicity, they reduce the interactions among the FG repeats, in particular for the relatively compact N-terminal regions of Nsp1[39]. Second, by eliminating the FG motifs, they disrupt their FG-mediated interactions with NTRs[91]. We quantified permeability to passive diffusion by simulating transport using the same pore geometry and estimated grafting density as in the original study[91], but using the same representation and parameters for the FG repeats, passively diffusing molecules, and NTR:cargo complexes as in our current simulations. The resulting model reproduced the increase in passive permeability of the Nsp1-S nanopores for a molecule of a given size[91] (**Extended Data Fig. 6**, blue *vs* red). Our model also predicts that passive diffusion remains size-dependent even for Nsp1-S, with the permeability increasing by an order of magnitude.

We hypothesized that a rise in permeability due to a loss of FG:FG interactions can be alleviated by alternative mechanisms of transport selectivity, exemplifying resilience of the nucleocytoplasmic transport through the NPC. For example, the NTR-centric (Kap-centric) model of transport[77,133,134] posits that the large populations of NTRs in the central transporter[4,76] directly contributes to size-dependence of passive diffusion. In agreement, our model predicts that the rise in permeability to passive diffusion is reversed by re-introduction of NTR binding (but not FG:FG interactions) to Nsp1-S (**Extended Data Fig. 5,** green). This reversibility indicates that FG:FG interactions are not essential for transport selectivity on its own, but are rather one of several contributing factors that provide robustness and resilience to the size-dependent barrier, in concert with other mechanisms of resilience such as dynamically bound NTRs in the central transporter.

Model reproduces robustness of transport to FG Nup deletions

The relative insensitivity of transport to FG:FG interactions is consistent with the viability of mutant strains with FG Nup deletions[135], exemplifying robustness of the nucleocytoplasmic transport through the NPC. This insensitivity is also consistent with the relatively modest changes in passive and facilitated diffusion in these strains[7]. To study the robustness of NPC transport to FG Nup deletions, we simulated transport through the NPC without Nsp1, removing 32% of the FG repeat mass. These NPC mutants retained both size-dependence and selectivity of transport (**Fig. 8c**). This prediction is validated by *in vivo* experimental measurements of passive and facilitated diffusion for the nsp1$^{\Delta FG}$ mutant strain[7], and is consistent with the size-dependence and selectivity of transport through NPC mimics with a single type of FG repeat[66,91,136]. The robustness of the NPC to changes in its FG Nup composition may be key to its ability to evolve gradually and adapt to diverse needs of different types of eukaryotic cells[137].

NPC dilation increases NPC permeability

We assessed whether the robustness of transport to variation in FG repeat identities, copy numbers, anchoring positions, and FG:FG interactions extends to variation of the NPC diameter. While early evidence for this variation[138,139] has been originally dismissed as spurious and without functional implications[139], additional evidence for its functional importance has been

mounting[32,62,72,79,80,140]. Thus, it was hypothesized that the dilation of the NPC plays a functional role in adaptations to internal and external stimuli, including mechanical stress, hyperosmotic shock, energy depletion[32,33,72], and development[141]. Interestingly, *in vivo* measurements of both passive and facilitated diffusion decreased markedly under cellular conditions coinciding with a constricted NPC[32,81], although implications for the structure-function relationship of the NPC remain uncertain due to the multitude of other concomitant phenomena[32]. Recently, it has been demonstrated using both experiment and simulation that artificial nanopores with increased diameter lead to faster translocation rates of Kap95 (facilitated diffusion) as well as BSA (passive diffusion), concomitant with an up to 8-fold increase in selectivity[66].

To assess the dependence of transport on the diameter of the central channel, we used a simplified cylinder pore model with only 32 chains of FG repeats[7], reminiscent of artificial NPC mimics previously used to study transport[66,91,136], in which we varied the pore radius from 13 to 25 nm in 1.5 nm increments; for each pore radius, 100-200 independent trajectories of 20 μs each were computed for both passive and facilitated diffusion, while keeping all other model parameters fixed. This model is based on our previous simplified model of passive diffusion[7], benefiting from better informed model parameters to describe the FG Nups and their interactions with the cargo:NTR complexes. The simplified model reproduces both transport selectivity and rates of the primary coarse-grained model studied here (**Fig. 8d-e;** *cf.* **Figs. 3a and 4g**), further demonstrating the robustness of transport to large perturbations of NPC architecture and composition.

The permeability to facilitated diffusion increases incrementally but substantially as the radius of the NPC increased, growing by almost 10-fold as the radius increased from 13 to 25 nm (**Fig. 8d**). Passive diffusion increases even more significantly; its size-dependence is maintained, but passive permeability increases more significantly for larger than smaller molecules, decreasing the downward slope of the permeability *vs* molecular weight curve as the pore radius increases (**Fig. 8e**). We conclude that the dilation of NPCs *in vivo* may indeed explain the increase in the NPC permeability under conditions such as energy depletion, osmotic shock, mechanical stress, and others[32,33,72].

The transport system is designed for robustness and resilience

After validating (**Figs. 1-2**) and dissecting (**Figs. 3-8**) our model, we are now in a position to discuss the mechanism of transport and the design features that lead to its robustness and resilience. Robustness allows the transport system to function under a range of conditions, while resilience allows it to quickly recover from or adapt to a disruption.

In our reductionist model, the nucleocytoplasmic transport arises from the composition of the system and interactions between its components; thus, the model avoids making circular phenomenological assumptions about key emergent properties of the transport. Nevertheless, the model reproduces these properties after its parameters are fit to experimental data and

theoretical information, allowing us to dissect how these properties emerge from the interactions between the system components.

Specifically, our model is consistent with some key aspects of the virtual gating model[36]. The virtual gate consists of a pore lined with flexible polymers forming a size-dependent entropic barrier to passive diffusion (**Fig. 3**); these flexible polymers transiently interact with NTR:cargo complexes to reduce the free energy barrier of facilitated diffusion (**Figs. 4-6**). Our model is consistent with the FG repeats in a dynamic state stabilized by its high configurational entropy[7,36,37,41,55,74] (**Supplementary Video 1**). An aspect of this dynamic state is the entropic repulsion near the NPC scaffold that explains the thin connections in sub-tomograms and simulations (**Fig. 2a-c; Extended Data Fig. 3**). However, some of the microscopic details that lead to the presumed emergent behavior are guessed qualitatively and some are left unspecified[36]. Therefore, the original virtual gating model cannot by itself explain mechanistically how the emergent properties result from the interactions among the components. In contrast, our modeling reveals seven features of transport design working in unison to confer robustness and resilience to virtual gating, as follows.

The first design feature is the 'fuzzy' and transient interactions between FG repeats and the cargo:NTR complexes as described by the anisotropic slide-and-exchange model[34,50]; 'fuzziness' denotes a highly-dynamic interacting state with an ensemble of rapidly interconverting conformers[34,142] (**Fig. 1fg; Fig. 4**). This design feature increases the exchange rate of interacting FG repeats and NTRs without reducing the avidity[47,48] (**Fig. 1f-g**), thereby enhancing both the selectivity and rate of facilitated diffusion by over an order of magnitude compared to less 'fuzzy' isotropic interactions (**Fig. 4i**, pink). . A 'fuzzy' interaction between FG repeats and cargo:NTR complexes may also contribute to the resilience of the native NPC to clogging by slow exchanging cargo:NTR complexes.

The second design feature is the valency of NTR:cargo complexes, corresponding to multiple non-overlapping binding sites for FG repeats on a single NTR molecule (**Fig. 6a-b**). This feature enhances both the selectivity and rate of facilitated diffusion for multivalent cargo:NTR complexes by several orders of magnitude compared with monovalent cargo:NTR complexes (**Fig. 6a-b**), due to multiple relatively weak interaction sites increasing the avidity without compromising the exchange rate (**Fig. 1g**). The ability to increase the avidity without compromising molecular exchange, conferred by both 'fuzziness' and multivalency of the FG repeat:NTR interactions, is critical to the robust transport of a wide range of molecular cargos, including large pre-ribosomal subunits (**Fig. 6**) and capsid-like particles (**Fig. 7**).

The third design feature is the 'fuzzy' and transient interactions between pairs of FG repeats (**Fig. 8a-b; Extended Data Fig. 6**). This feature enhances selectivity by reducing the rate of passive diffusion more strongly than for facilitated diffusion (**Fig. 8a-b**, green *vs* yellow). Nonetheless, overly strong FG:FG interactions may be detrimental to selectivity (**Fig. 8b**). Thus, the 'fuzzy' nature of the FG:FG interactions[142] is critical for the enhancement of selectivity. Indeed, the model of the wildtype NPC is in agreement with experimental data on

size-dependent passive diffusion (**Fig. 3a; Extended Data Fig. 3a**) without recourse to stronger interactions assumed in a model of saturated hydrogel[42]. Moreover, the model predicts that transport would be selective even without any FG:FG interactions (**Fig. 8b,** green).

The fourth design feature is the presence of NTRs in the central transporter[77,133,134] (**Extended Data Fig. 6**, green). This feature enhances selectivity by reducing the rates of passive diffusion. The NTRs contribute to the robustness of the size-dependent barrier, for example by reversing the increase in permeability due to loss of 'fuzzy' FG:FG interactions.

The fifth design feature is redundancy in the copy number of FG Nups (**Fig. 8c**). This feature enhances the resilience to evolutionary deletions and mutations of FG Nups, because the transport system is already selective for a low copy number of FG Nups, corresponding to robustness with regard to FG Nup composition.

The sixth design feature is the exponential coupling of transport kinetics and thermodynamics in accordance with the transition state theory[7,116,117] (**Fig. 3c-f; Fig. 4c-d; Fig. 5c-e; Extended Data Fig. 4c**); TST predicts that reaction rates decrease exponentially with the magnitude of an energy barrier for passive diffusion (**Fig. 3f)**, but increase exponentially as the energy barrier is lowered as a result of FG repeat:NTR interactions for facilitated diffusion (**Fig. 4-5**). This feature thus enhances transport selectivity, and helps rationalize the NPC's ability to facilitate the transport of megadalton cargo molecules as large as pre-ribosomal subunits through the transient energetic contributions from only a few NTRs (**Fig. 6-7**), while inhibiting the passive diffusion of molecules as small as a few dozen kDa (**Fig. 3**).

The seventh design feature is a consequential result of the otherwise well-established coupling of facilitated diffusion to the concentration gradient of RanGTP[143] (**Fig. 7; Extended Data Fig. 5**). This feature enhances the transport rates for large cargo:NTR complexes even when the permeability saturates as a function of valency at the single NPC level (**Fig. 7**). Thus, it enhances the robustness of transport, as it prevents permeability from becoming a bottleneck for transport of very large cargos. We demonstrate this feature by the coupling[50] of our spatiotemporal model of transport through a single NPC to a kinetic model of transport in the cell[72], allowing us to explain the empirical relationship between transport rates of large cargo and valency[75].

In conclusion, the model reveals how key emergent properties of transport, including rate, size-dependence of the rate, and selectivity, arise from the system components and their interactions, in a robust and resilient fashion with regard to environmental fluctuations and evolutionary pressures. Consideration of this robustness and resilience may allow us to rationally modulate and control the transport system or artificial mimics inspired by it.

Relation to other types of biophysical systems

The NPC is a unique cellular apparatus that acts as the gateway to the nucleus. Its architecture and function have been remarkably conserved across all eukaryotes[62] since it originated presumably in the last eukaryotic common ancestor 2.7 billion years ago[137] (**Fig. 3a; Extended**

Data Fig. 4a-b). The NPC must selectively transport cargoes of diverse chemistry, shape, and size. The design of the NPC must therefore be tailored to perform these roles robustly and resiliently with regard to the environmental noise and evolutionary perturbations. We next contrast the NPC with several other types of biophysical systems, including polymer brushes[37,74], biomolecular condensates[144], and saturated hydrogels[42].

Polymer brushes are commonly defined as polymer chains densely tethered to another polymer chain or surface[37,74]. Similarly to polymer brushes, the end-to-end distance of the FG repeats in our model increases upon grafting in the central channel (**Extended Data Fig. 2b**). This phenomenon was proposed as a possible basis for an entropically-driven selectivity barrier[37,74] involved in virtual gating as discussed above.

Biomolecular condensates are loosely defined as micron-scale compartments in eukaryotic cells that lack surrounding membranes, but concentrate biomolecules including proteins and nucleic acids[144]. This rather broad definition includes a diverse group of biophysical systems in different states[3,145,146]. Several transport models propose that the central transporter shares unusual viscoelastic properties with gels, hydrogels, and liquid-liquid phase separations[3,42,147–149]. We next consider transport system properties shared with condensates. In the NPC, the scaffold constrains the FG repeats into the relatively narrow space of the central channel through their specific anchoring to the scaffold; thus, the central transporter resembles the concentrated biomolecules in a condensate. In addition, our model is consistent with FG repeats driving the recruitment of a population of NTRs and cargo molecules to the NPC[4,76,77,133,134] (**Fig. 2**), similarly to the common description of condensate 'scaffold' proteins concentrating 'client' protein[145]. Moreover, our model suggests that the physical interactions among FG repeats and NTRs inside the central channel are highly dynamic, perhaps resembling a liquid-like state of condensates. Our model can accommodate - but does not depend upon - a modest level of 'fuzzy' intermolecular interactions between some FG repeats (**Fig. 8a-b**; **Extended Data Fig. 6**). Even with attractive FG:FG interactions, the FG repeats remain highly dynamic and rapidly exchanging with NTRs[47,48], courtesy of the slide-and-exchange mechanism[50] (**Fig. 1f-g**; **Fig. 4i**).

Saturated hydrogels are loosely defined as cross-linked networks of hydrophilic polymer materials that quickly absorb and retain water[42]. They may be considered a specific case of a biomolecular condensate[150]. Similarly to condensates, they cover a diverse group of materials. In the context of the NPC, FG repeats were originally suggested to form a sieve-like hydrogel with a mesh size of approximately 30 kDa for unhindered passive diffusion, providing a firm barrier toward inert molecules[42]. However, this model is inconsistent with the gradual decrease in permeability to passive diffusion in various cell types *in vivo*, including for molecules larger than 30-60 kDa[6,7,81] (**Fig. 3a; Extended Data Fig. 4a**). The hydrogel model also requires sufficiently strong FG:FG interactions to form the sieve, which may be inconsistent with the highly dynamic nature of FG repeats observed in recent *in situ* experiments[74] and our model (**Extended Data Fig. 2b**) as well as the ability of the central transporter to efficiently translocate megadalton cargo with the aid of relatively few NTRs[75] (**Fig. 4-6**).

Conclusions

Our reductionist spatiotemporal map of transport was trained and validated by a wide range of empirical observations on the biochemistry, morphology, and function of the NPC. The model enabled us to dissect key aspects of the transport mechanism and quantify their relative contributions to its functional integrity. The model is a rigorous quantitative starting point for more detailed characterizations of how to rationally modulate and control the transport system or artificial mimics inspired by it. In addition, the present study illustrates how our integrative experimental and computational approach can produce insightful models for complex biomolecular processes that are refractory to single methods.

Methods

Experimental and computational methods are described in detail in Supplementary Methods.

Funding

Modeling activities were supported by the National Institutes of Health (NIH) grants R01 GM117212 (D.C.), P41 GM109824 and R01 GM112108 (M.P.R. and A.S.), and R01 GM083960 (A.S.). Our early Brownian dynamics simulations were performed on the Google Exacycle cloud computer from 2013 to 2014; we acknowledge Google salary support for D.R. from 2013 to 2014. Molecular dynamics simulations were also performed on the Anton2 special-purpose supercomputer provided by the National Resource for Biomedical Supercomputing (NRBSC) courtesy of D.E. Shaw Research, the Pittsburgh Supercomputing Center (PSC), and the Biomedical Technology Research Center for Multiscale Modeling of Biological Systems (MMBioS) through grant P41GM103712-S1 from the NIH. SAXS data at NSLS was collected on the LiX beamline, part of the Center for BioMolecular Structure (CBMS), supported by NIH grants (P30GM133893, S10OD012331), and by the Department of Energy (DOE) Office of Biological and Environmental Research (KP1605010). Work performed at the CBMS was supported by the DOE Office of Science, Office of Basic Energy Sciences Program (DE-SC0012704). *In situ* cryo–ET of NPC was supported by NIH grants DP2 GM123494 and U54-AI170856 and NSF grant MRI DBI 1920374 (E.V.). E.V. is an investigator of the Howard Hughes Medical Institute. We acknowledge the use of the UC San Diego cryo-EM facility, which was built and equipped with funds from the University of California, San Diego and an initial gift from Agouron Institute. D.S. was supported by a Damon Runyon Postdoctoral Fellowship (DRG-2364-19) and is currently supported by the K99 Pathway to Independence Award from the NIH (K99AG080112). B.R. was supported by a Minerva center grant on Cell Intelligence.

Acknowledgements

We are most grateful to Dr. Frank Alber for initiating our Brownian dynamics simulations of nucleocytoplasmic transport in 2005, and to Dr. Lin Yang and staff at the LiX NSLS beamline for advice and assistance.

Ethics information

Nothing to declare.

Competing interests

All authors declare no competing interests.

References

1. Weis, K. Nucleocytoplasmic transport: cargo trafficking across the border. *Curr. Opin. Cell Biol.* **14,** 328–335 (2002).
2. Hoogenboom, B. W., Hough, L. E., Lemke, E. A., Lim, R. Y. H., Onck, P. R. & Zilman, A. Physics of the Nuclear Pore Complex: Theory, Modeling and Experiment. *Phys. Rep.* **921,** 1–53 (2021).
3. Cowburn, D. & Rout, M. Improving the hole picture: towards a consensus on the mechanism of nuclear transport. *Biochem. Soc. Trans.* **51,** 871–886 (2023).
4. Kim, S. J., Fernandez-Martinez, J., Nudelman, I., Shi, Y., Zhang, W., Raveh, B., Herricks, T., Slaughter, B. D., Hogan, J. A., Upla, P., Chemmama, I. E., Pellarin, R., Echeverria, I., Shivaraju, M., Chaudhury, A. S., Wang, J., Williams, R., Unruh, J. R., Greenberg, C. H., Jacobs, E. Y., Yu, Z., de la Cruz, M. J., Mironska, R., Stokes, D. L., Aitchison, J. D., Jarrold, M. F., Gerton, J. L., Ludtke, S. J., Akey, C. W., Chait, B. T., Sali, A. & Rout, M. P. Integrative structure and functional anatomy of a nuclear pore complex. *Nature* **555,** 475–482 (2018).
5. Ribbeck, K. & Gorlich, D. Kinetic analysis of translocation through nuclear pore complexes. *EMBO J.* **20,** 1320–1330 (2001).
6. Popken, P., Ghavami, A., Onck, P. R., Poolman, B. & Veenhoff, L. M. Size-dependent leak of soluble and membrane proteins through the yeast nuclear pore complex. *Mol. Biol. Cell* **26,** 1386–1394 (2015).
7. Timney, B. L., Raveh, B., Mironska, R., Trivedi, J. M., Kim, S. J., Russel, D., Wente, S. R., Sali, A. & Rout, M. P. Simple rules for passive diffusion through the nuclear pore complex. *J. Cell Biol.* **215,** 57–76 (2016).
8. Bayliss, R., Corbett, A. H. & Stewart, M. The molecular mechanism of transport of macromolecules through nuclear pore complexes. *Traffic* **1,** 448–456 (2000).
9. Feldherr, C. M. The effect of the electron-opaque pore material on exchanges through the nuclear annuli. *J. Cell Biol.* **25,** 43–53 (1965).
10. Stevens, B. J. & Swift, H. RNA transport from nucleus to cytoplasm in Chironomus salivary glands. *J. Cell Biol.* **31,** 55–77 (1966).
11. Paine, P. L., Moore, L. C. & Horowitz, S. B. Nuclear envelope permeability. *Nature* **254,** 109–114 (1975).
12. Feldherr, C. M., Kallenbach, E. & Schultz, N. Movement of a karyophilic protein through the nuclear pores of oocytes. *J. Cell Biol.* **99,** 2216–2222 (1984).
13. Mor, A., Suliman, S., Ben-Yishay, R., Yunger, S., Brody, Y. & Shav-Tal, Y. Dynamics of single mRNP nucleocytoplasmic transport and export through the nuclear pore in living cells. *Nat. Cell Biol.* **12,** 543–552 (2010).
14. Ibarra, A. & Hetzer, M. W. Nuclear pore proteins and the control of genome functions. *Genes Dev.* **29,** 337–349 (2015).
15. Akhtar, A. & Gasser, S. M. The nuclear envelope and transcriptional control. *Nat. Rev. Genet.* **8,** 507–517 (2007).
16. Strambio-De-Castillia, C., Niepel, M. & Rout, M. P. The nuclear pore complex: bridging nuclear transport and gene regulation. *Nat. Rev. Mol. Cell Biol.* **11,** 490–501 (2010).
17. Sumner, M. C. & Brickner, J. The Nuclear Pore Complex as a Transcription Regulator. *Cold Spring Harb. Perspect. Biol.* **14,** (2022).
18. Soheilypour, M. & Mofrad, M. R. K. Quality control of mRNAs at the entry of the nuclear pore: Cooperation in a complex molecular system. *Nucleus* **9,** 202–211 (2018).
19. Chatel, G. & Fahrenkrog, B. Nucleoporins: leaving the nuclear pore complex for a successful mitosis. *Cell. Signal.* **23,** 1555–1562 (2011).
20. Gu, Y., Zebell, S. G., Liang, Z., Wang, S., Kang, B.-H. & Dong, X. Nuclear Pore Permeabilization Is a Convergent Signaling Event in Effector-Triggered Immunity. *Cell* **166,** 1526–1538.e11 (2016).
21. Simon, D. N. & Rout, M. P. Cancer and the nuclear pore complex. *Adv. Exp. Med. Biol.* **773,** 285–307 (2014).
22. Kobiler, O., Drayman, N., Butin-Israeli, V. & Oppenheim, A. Virus strategies for passing the nuclear envelope barrier. *Nucleus* **3,** 526–539 (2012).
23. Diez, L. & Wegmann, S. Nuclear Transport Deficits in Tau-Related Neurodegenerative Diseases. *Front. Neurol.* **11,** 1056 (2020).
24. Chou, C.-C., Zhang, Y., Umoh, M. E., Vaughan, S. W., Lorenzini, I., Liu, F., Sayegh, M., Donlin-Asp, P. G., Chen, Y. H., Duong, D. M., Seyfried, N. T., Powers, M. A., Kukar, T., Hales, C. M., Gearing, M., Cairns, N. J., Boylan, K. B., Dickson, D. W., Rademakers, R., Zhang, Y.-J., Petrucelli, L., Sattler, R., Zarnescu, D. C., Glass, J. D. & Rossoll, W. TDP-43 pathology disrupts nuclear pore complexes and nucleocytoplasmic transport in ALS/FTD.

Nat. Neurosci. **21,** 228–239 (2018).
25. Tziortzouda, P., Van Den Bosch, L. & Hirth, F. Triad of TDP43 control in neurodegeneration: autoregulation, localization and aggregation. *Nature Reviews Neuroscience* **22,** 197–208 Preprint at https://doi.org/10.1038/s41583-021-00431-1 (2021)
26. Chowdhury, R., Sau, A. & Musser, S. M. Super-resolved 3D tracking of cargo transport through nuclear pore complexes. *Nat. Cell Biol.* **24,** 112–122 (2022).
27. Hoelz, A., Glavy, J. S. & Beck, M. Toward the atomic structure of the nuclear pore complex: when top down meets bottom up. *Nat. Struct. Mol. Biol.* **23,** 624–630 (2016).
28. Bui, K. H., von Appen, A., DiGuilio, A. L., Ori, A., Sparks, L., Mackmull, M.-T., Bock, T., Hagen, W., Andrés-Pons, A., Glavy, J. S. & Beck, M. Integrated structural analysis of the human nuclear pore complex scaffold. *Cell* **155,** 1233–1243 (2013).
29. Alber, F., Dokudovskaya, S., Veenhoff, L. M., Zhang, W., Kipper, J., Devos, D., Suprapto, A., Karni-Schmidt, O., Williams, R., Chait, B. T., Sali, A. & Rout, M. P. The molecular architecture of the nuclear pore complex. *Nature* **450,** 695–701 (2007).
30. Denning, D. P., Patel, S. S., Uversky, V., Fink, A. L. & Rexach, M. Disorder in the nuclear pore complex: the FG repeat regions of nucleoporins are natively unfolded. *Proc. Natl. Acad. Sci. U. S. A.* **100,** 2450–2455 (2003).
31. Schuller, A. P., Wojtynek, M., Mankus, D., Tatli, M., Kronenberg-Tenga, R., Regmi, S. G., Dip, P. V., Lytton-Jean, A. K. R., Brignole, E. J., Dasso, M., Weis, K., Medalia, O. & Schwartz, T. U. The cellular environment shapes the nuclear pore complex architecture. *Nature* **598,** 667–671 (2021).
32. Zimmerli, C. E., Allegretti, M., Rantos, V., Goetz, S. K., Obarska-Kosinska, A., Zagoriy, I., Halavatyi, A., Hummer, G., Mahamid, J., Kosinski, J. & Beck, M. Nuclear pores dilate and constrict in cellulo. *Science* **374,** eabd9776 (2021).
33. Elosegui-Artola, A., Andreu, I., Beedle, A. E. M., Lezamiz, A., Uroz, M., Kosmalska, A. J., Oria, R., Kechagia, J. Z., Rico-Lastres, P., Le Roux, A.-L., Shanahan, C. M., Trepat, X., Navajas, D., Garcia-Manyes, S. & Roca-Cusachs, P. Force Triggers YAP Nuclear Entry by Regulating Transport across Nuclear Pores. *Cell* **171,** 1397–1410.e14 (2017).
34. Sparks, S., Temel, D. B., Rout, M. P. & Cowburn, D. Deciphering the 'Fuzzy' Interaction of FG Nucleoporins and Transport Factors Using Small-Angle Neutron Scattering. *Structure* **26,** 477–484.e4 Preprint at https://doi.org/10.1016/j.str.2018.01.010 (2018)
35. Rout, M. P. & Sali, A. Principles for Integrative Structural Biology Studies. *Cell* **177,** 1384–1403 (2019).
36. Rout, M. P., Aitchison, J. D., Magnasco, M. O. & Chait, B. T. Virtual gating and nuclear transport: the hole picture. *Trends Cell Biol.* **13,** 622–628 (2003).
37. Lim, R. Y. H., Huang, N.-P., Köser, J., Deng, J., Lau, K. H. A., Schwarz-Herion, K., Fahrenkrog, B. & Aebi, U. Flexible phenylalanine-glycine nucleoporins as entropic barriers to nucleocytoplasmic transport. *Proc. Natl. Acad. Sci. U. S. A.* **103,** 9512–9517 (2006).
38. Wente, S. R. & Rout, M. P. The nuclear pore complex and nuclear transport. *Cold Spring Harb. Perspect. Biol.* **2,** a000562 (2010).
39. Yamada, J., Phillips, J. L., Patel, S., Goldfien, G., Calestagne-Morelli, A., Huang, H., Reza, R., Acheson, J., Krishnan, V. V., Newsam, S., Gopinathan, A., Lau, E. Y., Colvin, M. E., Uversky, V. N. & Rexach, M. F. A bimodal distribution of two distinct categories of intrinsically disordered structures with separate functions in FG nucleoporins. *Mol. Cell. Proteomics* **9,** 2205–2224 (2010).
40. Wagner, R. S., Kapinos, L. E., Marshall, N. J., Stewart, M. & Lim, R. Y. H. Promiscuous binding of Karyopherinβ1 modulates FG nucleoporin barrier function and expedites NTF2 transport kinetics. *Biophys. J.* **108,** 918–927 (2015).
41. Lim, R. Y. H., Fahrenkrog, B., Köser, J., Schwarz-Herion, K., Deng, J. & Aebi, U. Nanomechanical basis of selective gating by the nuclear pore complex. *Science* **318,** 640–643 (2007).
42. Frey, S. & Görlich, D. A saturated FG-repeat hydrogel can reproduce the permeability properties of nuclear pore complexes. *Cell* **130,** 512–523 (2007).
43. Peters, R. Translocation through the nuclear pore: Kaps pave the way. *Bioessays* **31,** 466–477 (2009).
44. Wälde, S. & Kehlenbach, R. H. The Part and the Whole: functions of nucleoporins in nucleocytoplasmic transport. *Trends Cell Biol.* **20,** 461–469 (2010).
45. Moussavi-Baygi, R., Jamali, Y., Karimi, R. & Mofrad, M. R. K. Brownian dynamics simulation of nucleocytoplasmic transport: a coarse-grained model for the functional state of the nuclear pore complex. *PLoS Comput. Biol.* **7,** e1002049 (2011).
46. Tagliazucchi, M., Peleg, O., Kröger, M., Rabin, Y. & Szleifer, I. Effect of charge, hydrophobicity, and sequence of

nucleoporins on the translocation of model particles through the nuclear pore complex. *Proceedings of the National Academy of Sciences* **110,** 3363–3368 (2013).
47. Milles, S., Mercadante, D., Aramburu, I. V., Jensen, M. R., Banterle, N., Koehler, C., Tyagi, S., Clarke, J., Shammas, S. L., Blackledge, M., Gräter, F. & Lemke, E. A. Plasticity of an ultrafast interaction between nucleoporins and nuclear transport receptors. *Cell* **163,** 734–745 (2015).
48. Hough, L. E., Dutta, K., Sparks, S., Temel, D. B., Kamal, A., Tetenbaum-Novatt, J., Rout, M. P. & Cowburn, D. The molecular mechanism of nuclear transport revealed by atomic-scale measurements. *Elife* **4,** (2015).
49. Zahn, R., Osmanović, D., Ehret, S., Araya Callis, C., Frey, S., Stewart, M., You, C., Görlich, D., Hoogenboom, B. W. & Richter, R. P. A physical model describing the interaction of nuclear transport receptors with FG nucleoporin domain assemblies. *Elife* **5,** (2016).
50. Raveh, B., Karp, J. M., Sparks, S., Dutta, K., Rout, M. P., Sali, A. & Cowburn, D. Slide-and-exchange mechanism for rapid and selective transport through the nuclear pore complex. *Proc. Natl. Acad. Sci. U. S. A.* **113,** E2489–97 (2016).
51. Knockenhauer, K. E. & Schwartz, T. U. The Nuclear Pore Complex as a Flexible and Dynamic Gate. *Cell* **164,** 1162–1171 (2016).
52. Aramburu, I. V. & Lemke, E. A. Floppy but not sloppy: Interaction mechanism of FG-nucleoporins and nuclear transport receptors. *Semin. Cell Dev. Biol.* **68,** 34–41 (2017).
53. Jovanovic-Talisman, T. & Zilman, A. Protein Transport by the Nuclear Pore Complex: Simple Biophysics of a Complex Biomachine. *Biophys. J.* **113,** 6–14 (2017).
54. Huang, K., Tagliazucchi, M., Park, S. H., Rabin, Y. & Szleifer, I. Nanocompartmentalization of the Nuclear Pore Lumen. *Biophys. J.* **118,** 219–231 (2020).
55. Winogradoff, D., Chou, H.-Y., Maffeo, C. & Aksimentiev, A. Percolation transition prescribes protein size-specific barrier to passive transport through the nuclear pore complex. *Nat. Commun.* **13,** 5138 (2022).
56. Zheng, T. & Zilman, A. Self-regulation of the nuclear pore complex enables clogging-free crowded transport. *Proc. Natl. Acad. Sci. U. S. A.* **120,** e2212874120 (2023).
57. Bayliss, R., Leung, S. W., Baker, R. P., Quimby, B. B., Corbett, A. H. & Stewart, M. Structural basis for the interaction between NTF2 and nucleoporin FxFG repeats. *EMBO J.* **21,** 2843–2853 (2002).
58. Port, S. A., Monecke, T., Dickmanns, A., Spillner, C., Hofele, R., Urlaub, H., Ficner, R. & Kehlenbach, R. H. Structural and Functional Characterization of CRM1-Nup214 Interactions Reveals Multiple FG-Binding Sites Involved in Nuclear Export. *Cell Rep.* **13,** 690–702 (2015).
59. Wing, C. E., Fung, H. Y. J. & Chook, Y. M. Karyopherin-mediated nucleocytoplasmic transport. *Nat. Rev. Mol. Cell Biol.* **23,** 307–328 (2022).
60. Isgro, T. A. & Schulten, K. Binding dynamics of isolated nucleoporin repeat regions to importin-beta. *Structure* **13,** 1869–1879 (2005).
61. Kosinski, J., Mosalaganti, S., von Appen, A., Teimer, R., DiGuilio, A. L., Wan, W., Bui, K. H., Hagen, W. J. H., Briggs, J. A. G., Glavy, J. S., Hurt, E. & Beck, M. Molecular architecture of the inner ring scaffold of the human nuclear pore complex. *Science* **352,** 363–365 (2016).
62. Akey, C. W., Singh, D., Ouch, C., Echeverria, I., Nudelman, I., Varberg, J. M., Yu, Z., Fang, F., Shi, Y., Wang, J., Salzberg, D., Song, K., Xu, C., Gumbart, J. C., Suslov, S., Unruh, J., Jaspersen, S. L., Chait, B. T., Sali, A., Fernandez-Martinez, J., Ludtke, S. J., Villa, E. & Rout, M. P. Comprehensive structure and functional adaptations of the yeast nuclear pore complex. *Cell* **185,** 361–378.e25 (2022).
63. Mosalaganti, S., Obarska-Kosinska, A., Siggel, M., Taniguchi, R., Turoňová, B., Zimmerli, C. E., Buczak, K., Schmidt, F. H., Margiotta, E., Mackmull, M.-T., Hagen, W. J. H., Hummer, G., Kosinski, J. & Beck, M. AI-based structure prediction empowers integrative structural analysis of human nuclear pores. *Science* **376,** eabm9506 (2022).
64. Eibauer, M., Pellanda, M., Turgay, Y., Dubrovsky, A., Wild, A. & Medalia, O. Structure and gating of the nuclear pore complex. *Nat. Commun.* **6,** 7532 (2015).
65. Mincer, J. S. & Simon, S. M. Simulations of nuclear pore transport yield mechanistic insights and quantitative predictions. *Proc. Natl. Acad. Sci. U. S. A.* **108,** E351–8 (2011).
66. Klughammer, N., Barth, A., Dekker, M., Fragasso, A., Onck, P. & Dekker, C. Diameter Dependence of Transport through Nuclear Pore Complex Mimics Studied Using Optical Nanopores. *Elife* 2023.02.18.529008 (2023).
67. Davis, L. K., Šarić, A., Hoogenboom, B. W. & Zilman, A. Physical modeling of multivalent interactions in the nuclear pore complex. *Biophys. J.* **120,** 1565–1577 (2021).
68. Zilman, A., Di Talia, S., Jovanovic-Talisman, T., Chait, B. T., Rout, M. P. & Magnasco, M. O. Enhancement of transport selectivity through nano-channels by non-specific competition. *PLoS Comput. Biol.* **6,** e1000804

(2010).
69. Zilman, A., Di Talia, S., Chait, B. T., Rout, M. P. & Magnasco, M. O. Efficiency, selectivity, and robustness of nucleocytoplasmic transport. *PLoS Comput. Biol.* **3,** e125 (2007).
70. Görlich, D., Seewald, M. J. & Ribbeck, K. Characterization of Ran-driven cargo transport and the RanGTPase system by kinetic measurements and computer simulation. *EMBO J.* **22,** 1088–1100 (2003).
71. Kim, S. & Elbaum, M. A simple kinetic model with explicit predictions for nuclear transport. *Biophys. J.* **105,** 565–569 (2013).
72. Andreu, I., Granero-Moya, I., Chahare, N. R., Clein, K., Molina-Jordán, M., Beedle, A. E. M., Elosegui-Artola, A., Abenza, J. F., Rossetti, L., Trepat, X., Raveh, B. & Roca-Cusachs, P. Mechanical force application to the nucleus regulates nucleocytoplasmic transport. *Nat. Cell Biol.* **24,** 896–905 (2022).
73. Huang, K., Tagliazucchi, M., Park, S. H., Rabin, Y. & Szleifer, I. Molecular model of the nuclear pore complex reveals a thermoreversible FG-network with distinct territories occupied by different FG motifs. *bioRxiv* (2019). at <https://www.biorxiv.org/content/10.1101/568865v1.abstract>
74. Yu, M., Heidari, M., Mikhaleva, S., Tan, P. S., Mingu, S., Ruan, H., Reinkemeier, C. D., Obarska-Kosinska, A., Siggel, M., Beck, M., Hummer, G. & Lemke, E. A. Visualizing the disordered nuclear transport machinery in situ. *Nature* **617,** 162–169 (2023).
75. Paci, G., Zheng, T., Caria, J., Zilman, A. & Lemke, E. A. Molecular determinants of large cargo transport into the nucleus. *Elife* **9,** (2020).
76. Lowe, A. R., Tang, J. H., Yassif, J., Graf, M., Huang, W. Y. C., Groves, J. T., Weis, K. & Liphardt, J. T. Importin-β modulates the permeability of the nuclear pore complex in a Ran-dependent manner. *eLife* **4,** Preprint at https://doi.org/10.7554/elife.04052 (2015)
77. Kapinos, L. E., Huang, B., Rencurel, C. & Lim, R. Y. H. Karyopherins regulate nuclear pore complex barrier and transport function. *J. Cell Biol.* **216,** 3609–3624 (2017).
78. Mohr, D., Frey, S., Fischer, T., Güttler, T. & Görlich, D. Characterisation of the passive permeability barrier of nuclear pore complexes. *EMBO J.* **28,** 2541–2553 (2009).
79. Mahamid, J., Pfeffer, S., Schaffer, M., Villa, E., Danev, R., Cuellar, L. K., Förster, F., Hyman, A. A., Plitzko, J. M. & Baumeister, W. Visualizing the molecular sociology at the HeLa cell nuclear periphery. *Science* **351,** 969–972 (2016).
80. Pulupa, J., Prior, H., Johnson, D. S. & Simon, S. M. Conformation of the nuclear pore in living cells is modulated by transport state. *Elife* **9,** (2020).
81. Andreu, I., Granero-Moya, I., Chahare, N. R. & Clein, K. Mechanosensitivity of nucleocytoplasmic transport. *bioRxiv* (2021). at <https://www.biorxiv.org/content/10.1101/2021.07.23.453478.abstract>
82. Ward, A. B., Sali, A. & Wilson, I. A. Biochemistry. Integrative structural biology. *Science* **339,** 913–915 (2013).
83. Russel, D., Lasker, K., Webb, B., Velazquez-Muriel, J., Tjioe, E., Schneidman-Duhovny, D., Peterson, B. & Sali, A. Putting the pieces together: integrative modeling platform software for structure determination of macromolecular assemblies. *PLoS Biol.* **10,** e1001244 (2012).
84. Braitbard, M., Schneidman-Duhovny, D. & Kalisman, N. Integrative Structure Modeling: Overview and Assessment. *Annual Review of Biochemistry* **88,** Preprint at https://doi.org/10.1146/annurev-biochem-013118-111429 (2019)
85. Sali, A. From integrative structural biology to cell biology. *Journal of Biological Chemistry* 100743 Preprint at https://doi.org/10.1016/j.jbc.2021.100743 (2021)
86. Alber, F., Dokudovskaya, S., Veenhoff, L. M., Zhang, W., Kipper, J., Devos, D., Suprapto, A., Karni-Schmidt, O., Williams, R., Chait, B. T., Rout, M. P. & Sali, A. Determining the architectures of macromolecular assemblies. *Nature* **450,** 683–694 (2007).
87. Raveh, B., Sun, L., White, K. L., Sanyal, T., Tempkin, J., Zheng, D., Bharath, K., Singla, J., Wang, C., Zhao, J., Li, A., Graham, N. A., Kesselman, C., Stevens, R. C. & Sali, A. Bayesian metamodeling of complex biological systems across varying representations. *Proc. Natl. Acad. Sci. U. S. A.* **118,** (2021).
88. Nachury, M. V. & Weis, K. The direction of transport through the nuclear pore can be inverted. *Proceedings of the National Academy of Sciences* **96,** 9622–9627 (1999).
89. Takizawa, C. G., Weis, K. & Morgan, D. O. Ran-independent nuclear import of cyclin B1-Cdc2 by importin beta. *Proc. Natl. Acad. Sci. U. S. A.* **96,** 7938–7943 (1999).
90. Hayama, R., Sparks, S., Hecht, L. M., Dutta, K., Karp, J. M., Cabana, C. M., Rout, M. P. & Cowburn, D. Thermodynamic characterization of the multivalent interactions underlying rapid and selective translocation through the nuclear pore complex. *J. Biol. Chem.* **293,** 4555–4563 (2018).
91. Ananth, A. N., Mishra, A., Frey, S., Dwarkasing, A., Versloot, R., van der Giessen, E., Görlich, D., Onck, P. &

Dekker, C. Spatial structure of disordered proteins dictates conductance and selectivity in nuclear pore complex mimics. *Elife* **7,** (2018).
92. Li, Z., Chen, S., Zhao, L., Huang, G., Xu, H., Yang, X., Wang, P., Gao, N. & Sui, S.-F. Nuclear export of pre-60S particles through the nuclear pore complex. *Nature* **618,** 411–418 (2023).
93. Kozai, T., Fernandez-Martinez, J., van Eeuwen, T., Gallardo, P., Kapinos, L. E., Mazur, A., Zhang, W., Tempkin, J., Panatala, R., Delgado-Izquierdo, M., Raveh, B., Sali, A., Chait, B. T., Veenhoff, L. M., Rout, M. P. & Lim, R. Y. H. Dynamic molecular mechanism of the nuclear pore complex permeability barrier. *bioRxiv* (2023). doi:10.1101/2023.03.31.535055
94. Ermak, D. L. & McCammon, J. A. Brownian dynamics with hydrodynamic interactions. *J. Chem. Phys.* **69,** 1352–1360 (1978).
95. Ando, T. & Skolnick, J. Sliding of proteins non-specifically bound to DNA: Brownian dynamics studies with coarse-grained protein and DNA models. *PLoS Comput. Biol.* **10,** e1003990 (2014).
96. McGuffee, S. R. & Elcock, A. H. Diffusion, crowding & protein stability in a dynamic molecular model of the bacterial cytoplasm. *PLoS Comput. Biol.* **6,** e1000694 (2010).
97. Lowe, A. R., Siegel, J. J., Kalab, P., Siu, M., Weis, K. & Liphardt, J. T. Selectivity mechanism of the nuclear pore complex characterized by single cargo tracking. *Nature* **467,** 600–603 (2010).
98. Schneidman-Duhovny, D., Pellarin, R. & Sali, A. Uncertainty in integrative structural modeling. *Curr. Opin. Struct. Biol.* **28,** 96–104 (2014).
99. Suter, D. M. Transcription Factors and DNA Play Hide and Seek. *Trends Cell Biol.* **30,** 491–500 (2020).
100. Shaw, D. E., Grossman, J. P., Bank, J. A., Batson, B., Butts, J. A., Chao, J. C., Deneroff, M. M., Dror, R. O., Even, A., Fenton, C. H., Forte, A., Gagliardo, J., Gill, G., Greskamp, B., Ho, C. R., Ierardi, D. J., Iserovich, L., Kuskin, J. S., Larson, R. H., Layman, T., Lee, L.-S., Lerer, A. K., Li, C., Killebrew, D., Mackenzie, K. M., Mok, S. Y.-H., Moraes, M. A., Mueller, R., Nociolo, L. J., Peticolas, J. L., Quan, T., Ramot, D., Salmon, J. K., Scarpazza, D. P., Schafer, U. B., Siddique, N., Snyder, C. W., Spengler, J., Tang, P. T. P., Theobald, M., Toma, H., Towles, B., Vitale, B., Wang, S. C. & Young, C. Anton 2: Raising the Bar for Performance and Programmability in a Special-Purpose Molecular Dynamics Supercomputer. in *SC '14: Proceedings of the International Conference for High Performance Computing, Networking, Storage and Analysis* 41–53 (2014).
101. Enenkel, C., Blobel, G. & Rexach, M. Identification of a yeast karyopherin heterodimer that targets import substrate to mammalian nuclear pore complexes. *J. Biol. Chem.* **270,** 16499–16502 (1995).
102. Ribbeck, K. NTF2 mediates nuclear import of Ran. *The EMBO Journal* **17,** 6587–6598 Preprint at https://doi.org/10.1093/emboj/17.22.6587 (1998)
103. Braun, I. C., Herold, A., Rode, M. & Izaurralde, E. Nuclear export of mRNA by TAP/NXF1 requires two nucleoporin-binding sites but not p15. *Mol. Cell. Biol.* **22,** 5405–5418 (2002).
104. Katahira, J., Dimitrova, L., Imai, Y. & Hurt, E. NTF2-like domain of Tap plays a critical role in cargo mRNA recognition and export. *Nucleic Acids Res.* **43,** 1894–1904 (2015).
105. Van Der Maarel, J. R. C. *Introduction To Biopolymer Physics*. (World Scientific Publishing Company, 2007).
106. Unwin, P. N. & Milligan, R. A. A large particle associated with the perimeter of the nuclear pore complex. *J. Cell Biol.* **93,** 63–75 (1982).
107. Lin, D. H., Stuwe, T., Schilbach, S., Rundlet, E. J., Perriches, T., Mobbs, G., Fan, Y., Thierbach, K., Huber, F. M., Collins, L. N., Davenport, A. M., Jeon, Y. E. & Hoelz, A. Architecture of the symmetric core of the nuclear pore. *Science* **352,** aaf1015 (2016).
108. Akey, C. W., Echeverria, I., Ouch, C., Nudelman, I., Shi, Y., Wang, J., Chait, B. T., Sali, A., Fernandez-Martinez, J. & Rout, M. P. Implications of a multiscale structure of the yeast nuclear pore complex. *Mol. Cell* **83,** 3283–3302.e5 (2023).
109. Rout, M. P., Aitchison, J. D., Suprapto, A., Hjertaas, K., Zhao, Y. & Chait, B. T. The yeast nuclear pore complex: composition, architecture, and transport mechanism. *J. Cell Biol.* **148,** 635–651 (2000).
110. Huang, K. & Szleifer, I. Modeling the nucleoporins that form the hairy pores. *Biochem. Soc. Trans.* **48,** 1447–1461 (2020).
111. Fiserova, J., Richards, S. A., Wente, S. R. & Goldberg, M. W. Facilitated transport and diffusion take distinct spatial routes through the nuclear pore complex. *J. Cell Sci.* **123,** 2773–2780 (2010).
112. Yang, W. Distinct, but not completely separate spatial transport routes in the nuclear pore complex. *Nucleus* **4,** 166–175 (2013).
113. Brown, D. D. A tribute to the Xenopus laevis oocyte and egg. *J. Biol. Chem.* **279,** 45291–45299 (2004).
114. Bonner, W. M. Protein migration into nuclei. II. Frog oocyte nuclei accumulate a class of microinjected oocyte nuclear proteins and exclude a class of microinjected oocyte cytoplasmic proteins. *J. Cell Biol.* **64,** 431–437

(1975).
115. Nguyen, T., Pappireddi, N. & Wühr, M. Proteomics of nucleocytoplasmic partitioning. *Curr. Opin. Chem. Biol.* **48,** 55–63 (2019).
116. Eyring, H. The Activated Complex in Chemical Reactions. *J. Chem. Phys.* **3,** 107–115 (1935).
117. Evans, M. G. & Polanyi, M. Some applications of the transition state method to the calculation of reaction velocities, especially in solution. *Transactions of the Faraday Society* **31,** 875–894 (1935).
118. Burada, P. S., Hänggi, P., Marchesoni, F., Schmid, G. & Talkner, P. Diffusion in confined geometries. *Chemphyschem* **10,** 45–54 (2009).
119. Zumbro, E., Witten, J. & Alexander-Katz, A. Computational Insights into Avidity of Polymeric Multivalent Binders. *Biophys. J.* **117,** 892–902 (2019).
120. Einstein, A. *Über einen die Erzeugung und Verwandlung des Lichtes betreffenden heuristischen Gesichtspunkt ; Über die von molekularkinetischen Theorie der Wärme geforderte Bewegung von in ruhenden Flüssigkeiten suspendierten Teilchen ; Zur Elektrodynamik bewegter Körper.* (J.A. Barth, 1905).
121. Stokes, G. G. & Royal College of Surgeons of England. *On the effect of the internal friction of fluids on the motion of pendulums*. (Legare Street Press, 1851).
122. Liu, S. M. & Stewart, M. Structural basis for the high-affinity binding of nucleoporin Nup1p to the Saccharomyces cerevisiae importin-beta homologue, Kap95p. *J. Mol. Biol.* **349,** 515–525 (2005).
123. Grant, R. P., Hurt, E., Neuhaus, D. & Stewart, M. Structure of the C-terminal FG-nucleoporin binding domain of Tap/NXF1. *Nat. Struct. Biol.* **9,** 247–251 (2002).
124. Fasting, C., Schalley, C. A., Weber, M., Seitz, O., Hecht, S., Koksch, B., Dernedde, J., Graf, C., Knapp, E.-W. & Haag, R. Multivalency as a chemical organization and action principle. *Angew. Chem. Int. Ed Engl.* **51,** 10472–10498 (2012).
125. Kiessling, L. L., Gestwicki, J. E. & Strong, L. E. Synthetic Multivalent Ligands as Probes of Signal Transduction. *ChemInform* **37,** Preprint at https://doi.org/10.1002/chin.200627272 (2006)
126. Erlendsson, S. & Teilum, K. Binding Revisited—Avidity in Cellular Function and Signaling. *Frontiers in Molecular Biosciences* **7,** Preprint at https://doi.org/10.3389/fmolb.2020.615565 (2021)
127. Davis, L. K., Šarić, A., Hoogenboom, B. W. & Zilman, A. Physical modelling of multivalent interactions in the nuclear pore complex. *bioRxiv* 2020.10.01.322156 (2020). doi:10.1101/2020.10.01.322156
128. Izaurralde, E., Kutay, U., von Kobbe, C., Mattaj, I. W. & Görlich, D. The asymmetric distribution of the constituents of the Ran system is essential for transport into and out of the nucleus. *EMBO J.* **16,** 6535–6547 (1997).
129. Rexach, M. & Blobel, G. Protein import into nuclei: association and dissociation reactions involving transport substrate, transport factors, and nucleoporins. *Cell* **83,** 683–692 (1995).
130. Cavazza, T. & Vernos, I. The RanGTP Pathway: From Nucleo-Cytoplasmic Transport to Spindle Assembly and Beyond. *Front Cell Dev Biol* **3,** 82 (2015).
131. Cautain, B., Hill, R., de Pedro, N. & Link, W. Components and regulation of nuclear transport processes. *FEBS J.* **282,** 445–462 (2015).
132. Gu, C., Vovk, A., Zheng, T., Coalson, R. D. & Zilman, A. The Role of Cohesiveness in the Permeability of the Spatial Assemblies of FG Nucleoporins. *Biophys. J.* **116,** 1204–1215 (2019).
133. Osmanović, D., Ford, I. J. & Hoogenboom, B. W. Model inspired by nuclear pore complex suggests possible roles for nuclear transport receptors in determining its structure. *Biophys. J.* **105,** 2781–2789 (2013).
134. Lim, R. Y. H., Huang, B. & Kapinos, L. E. How to operate a nuclear pore complex by Kap-centric control. *Nucleus* **6,** 366–372 (2015).
135. Strawn, L. A., Shen, T., Shulga, N., Goldfarb, D. S. & Wente, S. R. Minimal nuclear pore complexes define FG repeat domains essential for transport. *Nat. Cell Biol.* **6,** 197–206 (2004).
136. Jovanovic-Talisman, T., Tetenbaum-Novatt, J., McKenney, A. S., Zilman, A., Peters, R., Rout, M. P. & Chait, B. T. Artificial nanopores that mimic the transport selectivity of the nuclear pore complex. *Biophys. J.* **96,** 545a (2009).
137. DeGrasse, J. A., DuBois, K. N., Devos, D., Siegel, T. N., Sali, A., Field, M. C., Rout, M. P. & Chait, B. T. Evidence for a shared nuclear pore complex architecture that is conserved from the last common eukaryotic ancestor. *Mol. Cell. Proteomics* **8,** 2119–2130 (2009).
138. Kiseleva, E., Goldberg, M. W., Allen, T. D. & Akey, C. W. Active nuclear pore complexes in Chironomus: visualization of transporter configurations related to mRNP export. *J. Cell Sci.* **111 (Pt 2),** 223–236 (1998).
139. Feldherr, C. M., Akin, D. & Cohen, R. J. Regulation of functional nuclear pore size in fibroblasts. *J. Cell Sci.* **114,** 4621–4627 (2001).

140. Allegretti, M., Zimmerli, C. E., Rantos, V., Wilfling, F., Ronchi, P., Fung, H. K. H., Lee, C.-W., Hagen, W., Turoňová, B., Karius, K., Börmel, M., Zhang, X., Müller, C. W., Schwab, Y., Mahamid, J., Pfander, B., Kosinski, J. & Beck, M. In-cell architecture of the nuclear pore and snapshots of its turnover. *Nature* **586,** 796–800 (2020).
141. Sellés, J., Penrad-Mobayed, M., Guillaume, C., Fuger, A., Auvray, L., Faklaris, O. & Montel, F. Nuclear pore complex plasticity during developmental process as revealed by super-resolution microscopy. *Sci. Rep.* **7,** 14732 (2017).
142. Sharma, R., Raduly, Z., Miskei, M. & Fuxreiter, M. Fuzzy complexes: Specific binding without complete folding. *FEBS Lett.* **589,** 2533–2542 (2015).
143. Becskei, A. & Mattaj, I. W. The strategy for coupling the RanGTP gradient to nuclear protein export. *Proc. Natl. Acad. Sci. U. S. A.* **100,** 1717–1722 (2003).
144. Bestembayeva, A., Kramer, A., Labokha, A. A., Osmanović, D., Liashkovich, I., Orlova, E. V., Ford, I. J., Charras, G., Fassati, A. & Hoogenboom, B. W. Nanoscale stiffness topography reveals structure and mechanics of the transport barrier in intact nuclear pore complexes. *Nat. Nanotechnol.* **10,** 60–64 (2015).
145. Banani, S. F., Lee, H. O., Hyman, A. A. & Rosen, M. K. Biomolecular condensates: organizers of cellular biochemistry. *Nat. Rev. Mol. Cell Biol.* **18,** 285–298 (2017).
146. Martin, E. W. & Holehouse, A. S. Intrinsically disordered protein regions and phase separation: sequence determinants of assembly or lack thereof. *Emerg Top Life Sci* **4,** 307–329 (2020).
147. Hampoelz, B., Schwarz, A., Ronchi, P., Bragulat-Teixidor, H., Tischer, C., Gaspar, I., Ephrussi, A., Schwab, Y. & Beck, M. Nuclear Pores Assemble from Nucleoporin Condensates During Oogenesis. *Cell* **179,** 671–686.e17 (2019).
148. Mobbs, G. W. & Hoelz, A. Nucleoporin Condensates Drive Nuclear Pore Complex Assembly in Oocytes. *Trends Biochem. Sci.* **45,** 278–280 (2020).
149. Dekker, M., Van der Giessen, E. & Onck, P. R. Phase separation of intrinsically disordered FG-Nups is driven by highly dynamic FG motifs. *Proc. Natl. Acad. Sci. U. S. A.* **120,** e2221804120 (2023).
150. Nag, N., Sasidharan, S., Uversky, V. N., Saudagar, P. & Tripathi, T. Phase separation of FG-nucleoporins in nuclear pore complexes. *Biochim. Biophys. Acta Mol. Cell Res.* **1869,** 119205 (2022).
151. Ameismeier, M., Cheng, J., Berninghausen, O. & Beckmann, R. Visualizing late states of human 40S ribosomal subunit maturation. *Nature* **558,** 249–253 (2018).
152. Rambo, R. P. & Tainer, J. A. Characterizing flexible and intrinsically unstructured biological macromolecules by SAS using the Porod-Debye law. *Biopolymers* **95,** 559–571 (2011).
153. Sakiyama, Y., Mazur, A., Kapinos, L. E. & Lim, R. Y. H. Spatiotemporal dynamics of the nuclear pore complex transport barrier resolved by high-speed atomic force microscopy. *Nat. Nanotechnol.* **11,** 719–723 (2016).
154. Paci, G. & Lemke, E. A. Molecular determinants of large cargo transport into the nucleus. *bioRxiv* 695080 (2019). doi:10.1101/695080
155. Delavoie, F., Soldan, V., Rinaldi, D., Dauxois, J.-Y. & Gleizes, P.-E. The path of pre-ribosomes through the nuclear pore complex revealed by electron tomography. *Nat. Commun.* **10,** 497 (2019).
156. Denning, D., Mykytka, B., Allen, N. P., Huang, L., Al Burlingame & Rexach, M. The nucleoporin Nup60p functions as a Gsp1p-GTP-sensitive tether for Nup2p at the nuclear pore complex. *J. Cell Biol.* **154,** 937–950 (2001).
157. Dilworth, D. J., Suprapto, A., Padovan, J. C., Chait, B. T., Wozniak, R. W., Rout, M. P. & Aitchison, J. D. Nup2p dynamically associates with the distal regions of the yeast nuclear pore complex. *J. Cell Biol.* **153,** 1465–1478 (2001).
158. Fischer, H., Polikarpov, I. & Craievich, A. F. Average protein density is a molecular-weight-dependent function. *Protein Sci.* **13,** 2825–2828 (2004).
159. Erickson, H. P. Size and shape of protein molecules at the nanometer level determined by sedimentation, gel filtration, and electron microscopy. *Biol. Proced. Online* **11,** 32–51 (2009).
160. Lemke, E. A. The Multiple Faces of Disordered Nucleoporins. *J. Mol. Biol.* **428,** 2011–2024 (2016).
161. Maragliano, L. & Vanden-Eijnden, E. A temperature accelerated method for sampling free energy and determining reaction pathways in rare events simulations. *Chem. Phys. Lett.* **426,** 168–175 (2006).
162. Abrams, C. F. & Vanden-Eijnden, E. Large-scale conformational sampling of proteins using temperature-accelerated molecular dynamics. *Proc. Natl. Acad. Sci. U. S. A.* **107,** 4961–4966 (2010).
163. Petrucci, R. H., Petrucci, R., Geoffrey Herring, F., Madura, J. & Bissonnette, C. *General Chemistry: Principles and Modern Applications*. (Pearson, 2017).
164. Molines, A. T., Lemière, J., Gazzola, M., Steinmark, I. E., Edrington, C. H., Hsu, C.-T., Real-Calderon, P., Suhling, K., Goshima, G., Holt, L. J., Thery, M., Brouhard, G. J. & Chang, F. Physical properties of the

cytoplasm modulate the rates of microtubule polymerization and depolymerization. *Dev. Cell* **57,** 466–479.e6 (2022).
165. Wagner, F. R., Watanabe, R., Schampers, R., Singh, D., Persoon, H., Schaffer, M., Fruhstorfer, P., Plitzko, J. & Villa, E. Preparing samples from whole cells using focused-ion-beam milling for cryo-electron tomography. *Nat. Protoc.* **15,** 2041–2070 (2020).
166. Mastronarde, D. N. Automated electron microscope tomography using robust prediction of specimen movements. *J. Struct. Biol.* **152,** 36–51 (2005).
167. Tegunov, D. & Cramer, P. Real-time cryo-electron microscopy data preprocessing with Warp. *Nat. Methods* **16,** 1146–1152 (2019).
168. Zheng, S., Wolff, G., Greenan, G., Chen, Z., Faas, F. G. A., Bárcena, M., Koster, A. J., Cheng, Y. & Agard, D. A. AreTomo: An integrated software package for automated marker-free, motion-corrected cryo-electron tomographic alignment and reconstruction. *J Struct Biol X* **6,** 100068 (2022).
169. Scheres, S. H. W. RELION: implementation of a Bayesian approach to cryo-EM structure determination. *J. Struct. Biol.* **180,** 519–530 (2012).

Figures

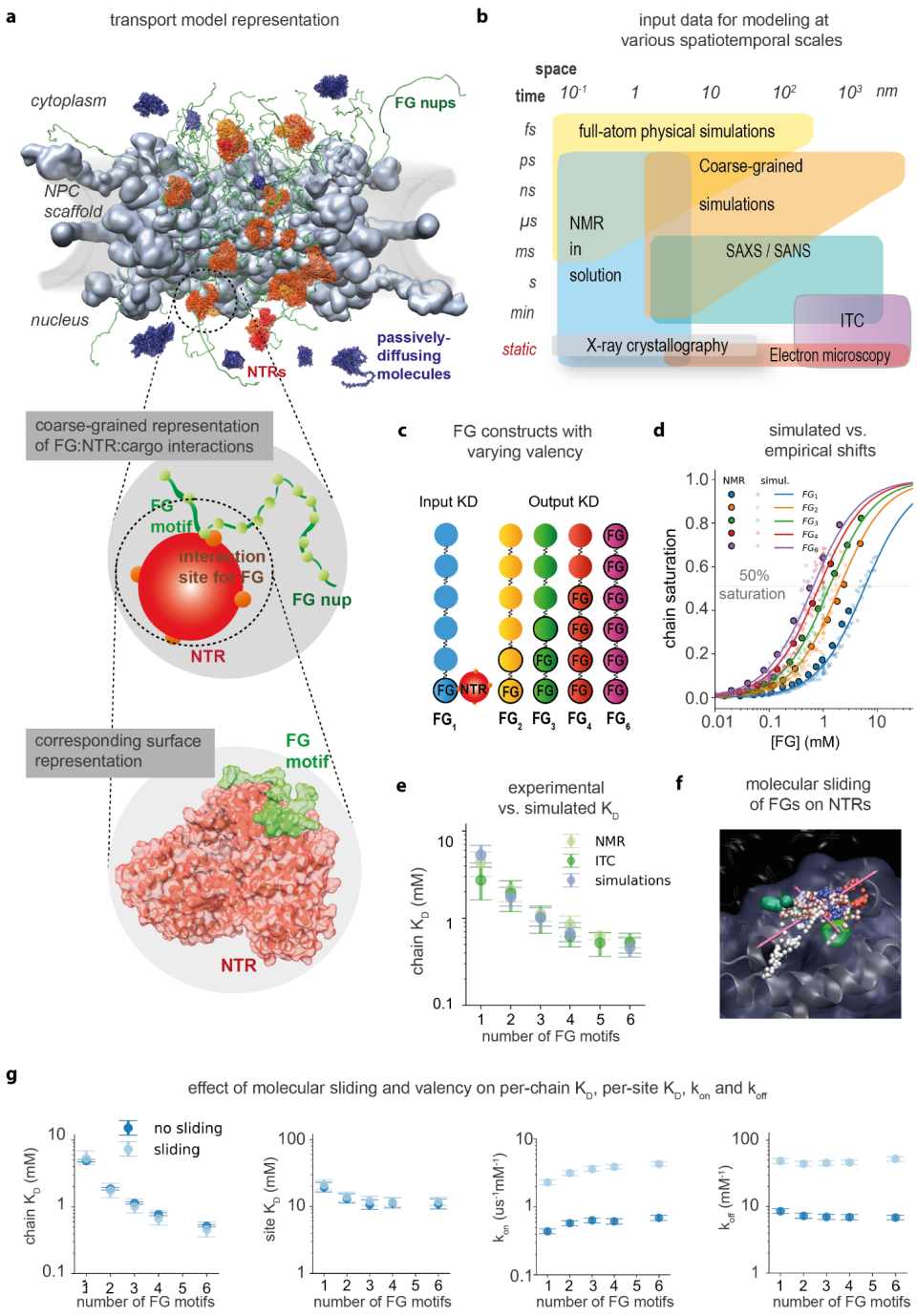

Fig. 1. Integrative spatiotemporal modeling of nucleocytoplasmic transport.

a, Representation of the transport model. **b,** Spatiotemporal scales of the input information for modeling. **c,** FG repeat constructs used here *in silico* and previously *in vitro*[90] to assess the effect of their valency on FG motif:NTR interactions. Each circle represents a segment of 20 amino acid residues. Segments labeled "FG" contain a single FSFG motif. The FSFG motifs in unlabeled segments were mutated to SSSG and therefore do not interact with NTRs. **d,** Simulated (here) and experimental[90] titration curves of NTR chemical shifts (y-axis) as a function

of the concentration of FG constructs with varying valencies (**c**; x-axis) at a fixed concentration of NTR molecules (NTF2, 10 uM). **e,** Per-chain K_D values for the interaction between an FG construct and NTF2 as a function of FG valency in NMR or ITC experiments (light and dark green, respectively)[90] and in the model (purple-blue). **f,** Sliding of an FG motif interacting with a karyopherin, shown in a snapshot from an al-atom simulation on the Anton 2 supercomputer[100] of a construct of six FG repeats interacting with Kap95. The pink spheres indicate the centers of mass of interacting FG motifs. The arrows indicate a principal component analysis of these centers of mass, indicating an anisotropic sliding of the FG motifs on the interhelical groove formed between the HEAT repeats of Kap95, similar to our result for NTF2[50]. **g,** Per-chain K_D, per-site K_D, k_{on}, and k_{off} values for the interactions between an NTR molecule (NTF2) and multivalent FG construct as a function of FG valency, with and without a sliding interaction potential. Even though the per-chain and per-site K_D values are nearly identical for the sliding and non-sliding potentials for any FG valency, the per-site exchange rates k_{on} and k_{off} are an order magnitude higher for the sliding potential than for the non-sliding potential.

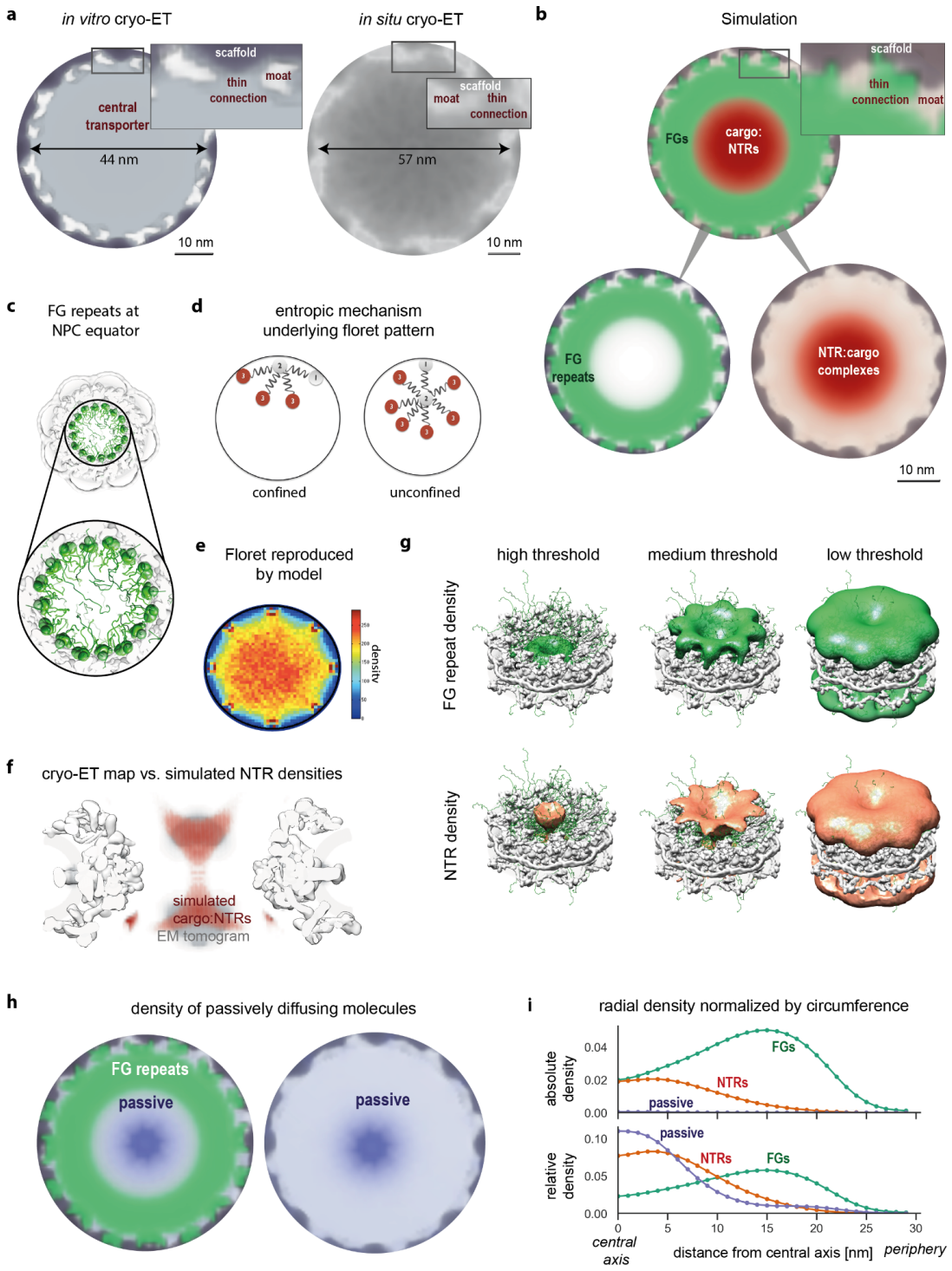

Fig. 2. Morphology of the central transporter and spatial routes of transport.

a, Density at the central channel (viewed from the cytoplasm) at the midpoint of the nuclear envelope from the *in vitro* cryo-ET map of isolated NPCs[4] and *in situ* cryo ET map shown in gray. The scaffold density in the *in vitro* map is shown in black-gray. **b,** Same as in **a**, but for simulated densities of the FG repeats (green) and NTRs (orange-red) near the equator of the central transporter. The scaffold of the NPC from the cryo-ET map[4] is shown in gray-black as in **a**, without the central transporter. **c,** The floret pattern for the density of a single layer of eight

FG Nups with 15 FG repeats each anchored to a cylinder with the radius of 20 nm indicates that the floret in the cryo-ET map and NPC model is an inherent feature of disordered polymer chains anchored to the walls of a cylinder. **d,** Illustration of an entropic mechanism proposed to result in the floret: The number of polymer chain configurations is smaller when its stem is closer to the scaffold. **e,** Snapshot from a simulation showing FG repeat domains (green tube representation) projecting from their anchor domains (green surface) near the equator of the NPC scaffold (white surface)[4]. **f,** A side view of the NPC scaffold (white surface) with high-density lobes in the simulated NTRs (red) and in the cryo-ET map (gray)[4]. **g,** FG repeat and NTR densities contoured at three increasingly lower density thresholds, from left to right, inside the NPC scaffold[4]. **h,** Density of passively diffusing molecules (purple-blue) and FG repeats (green) at the equator of the central channel; because the density of passively diffusing molecules is low, the density threshold for the passively diffusing molecules is approximately 100 times lower than in **b**. **i,** Densities of FG repeats (green), cargo-carrying NTRs (red), and passively diffusing molecules (purple-blue) in the central transporter as a function of distance from the NPC central axis, computed from the corresponding radial densities divided by the radius, to account for the increasing circumference at the periphery. In the top panel, the density of all three series sums to 1, whereas in the bottom panel, the density of each series sums to 1. The overall density of passively diffusing molecules is significantly lower than those of NTRs (top); in addition, passively diffusing molecules tend to diffuse closer to the central axis of the NPC than the NTRs (bottom).

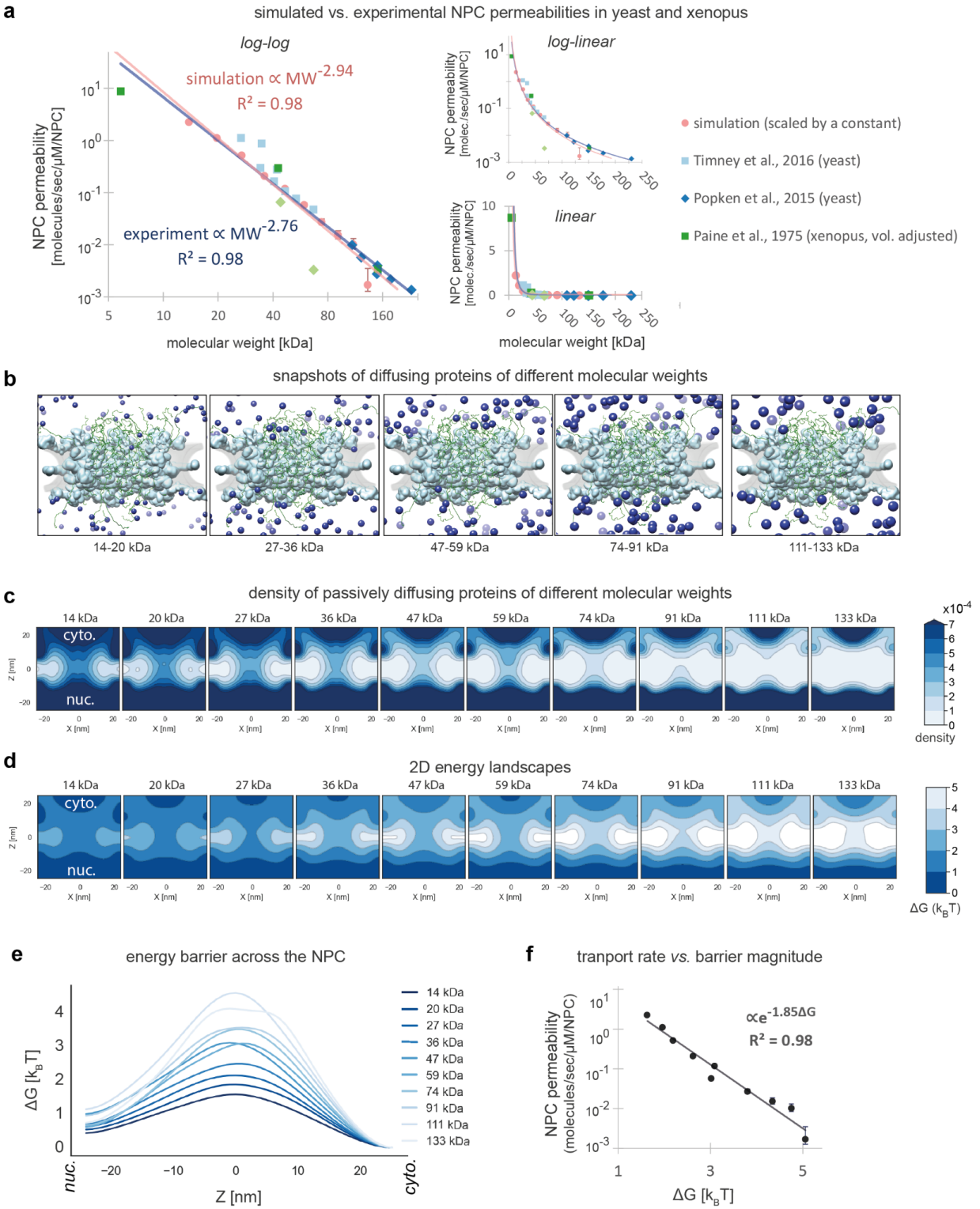

Fig. 3. Size-dependent kinetics and thermodynamics of passive diffusion.

a, Comparison of simulated NPC permeabilities (pink) and experimental permeabilities from *in vivo* measurements in yeast[6,7] (blue shades) and Xenopus[11,114] (green shades). The simulated permeability values are scaled by a single free parameter to fit the yeast data. The Xenopus data are scaled by adjusting for the significantly larger cytoplasm and nucleus volume in

Xenopus (text). The pink and blue lines are power-law curves fitted to the simulated and experimental measurements in yeast, respectively. **b,** Snapshots showing passively diffusing molecules of different sizes (blue), matching the sizes for the two aligned panels in **a**. **c,** The density of passively diffusing molecules of varying molecular weights, in the *X*,*Z* plane at *Y*=0. **d,** Gibbs free energy landscape over a 2D cross-section of the NPC for passively diffusing molecules of different sizes, corresponding to the densities in **c**. **e,** Gibbs free energy for passively diffusing molecules of different sizes as a function of *Z* (integrated over the *X*,*Y* plane). **f,** NPC permeabilities as a function of the free energy barrier for passively diffusing molecules of different size in **e**, scaled by the same single free parameter as in **a**.

C

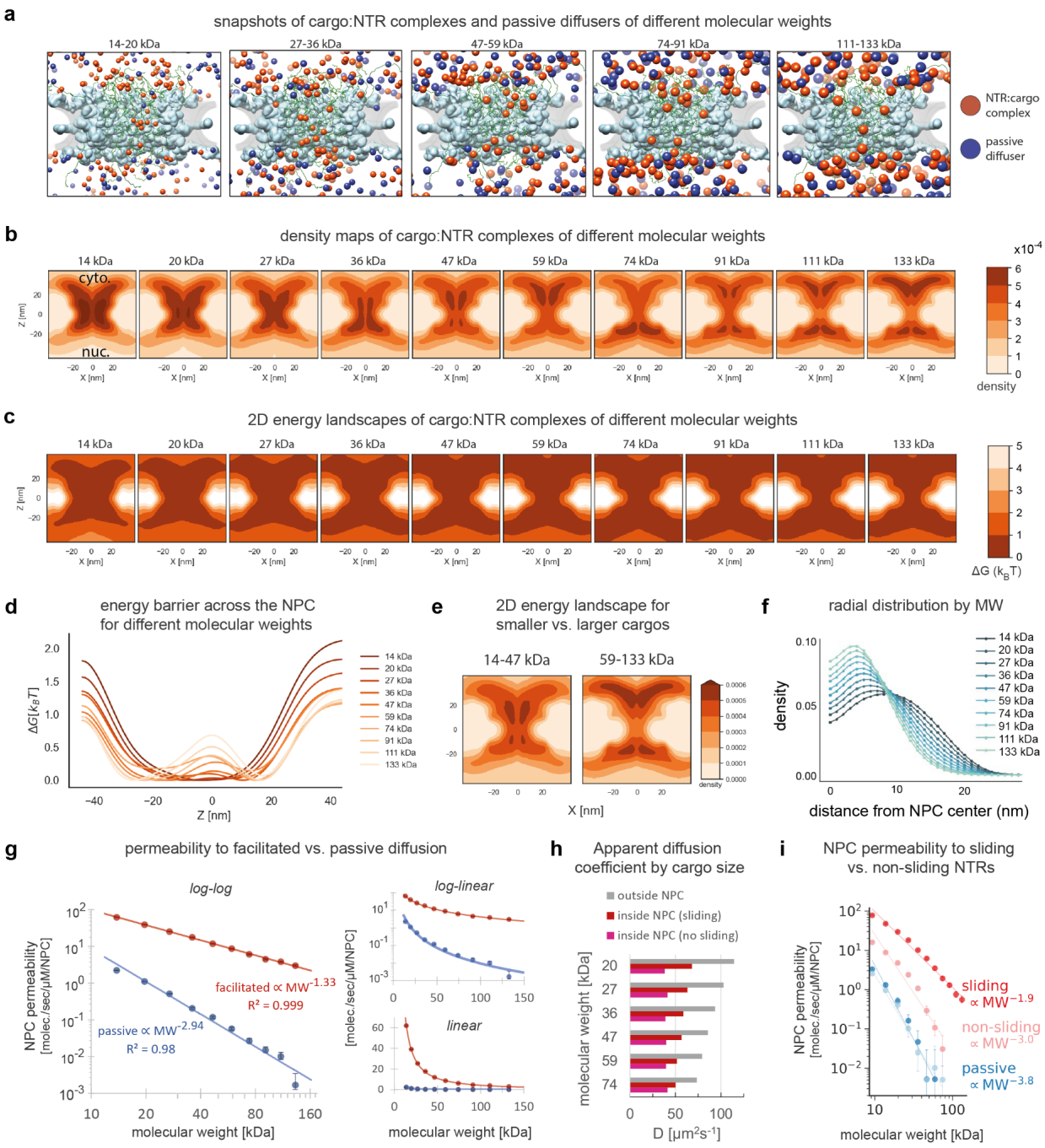

Fig. 4. Size-dependent kinetics and thermodynamics of facilitated diffusion.

a, A simulation snapshot showing both NTR:cargo complexes (orange-red) and passively diffusing molecules (blue) of different molecular weights. The molecular weight in each panel corresponds to the two panels above it in **a**. **b,** Simulated density over an *X/Z* cross-section of the NPC at *Y*=0 for NTR:cargo complexes of fixed FG valency (4 interaction sites) but different molecular weights. **c**, Gibbs free energy landscape over a 2D cross-section of the NPC for NTR:cargo complexes of different molecular weights, computed using a Boltzmann inversion of the probability densities in **a**. **d,** Gibbs free energy for NTR:cargo complexes translocating

across the NPC for molecules of different weight, obtained by integrating across the *X* and *Y* dimensions of their densities followed by a Boltzmann inversion. These simulations do not include the RanGTP cycle; they quantify the permeability of the NPC in the absence of any energy exchange with the environment of the simulated system. **e,** The density of small *vs* large NTR:cargo complexes. **f,** Densities of NTR:cargo complexes of different molecular weights as a function of their distance from the NPC central axis, computed as in **Fig. 2i**. **g,** NPC permeability as a function of molecular weight for facilitated *vs* passive diffusion (red *vs* blue, respectively). **h,** Apparent diffusion coefficients of molecules of different molecular weights outside (gray) *vs* inside the central channel, with (red) or without sliding (magenta) of cargo:NTR complexes. **i**, NPC permeability as a function of molecular weight for sliding (red, facilitated; blue, passive) *vs* non-sliding (pink, facilitated; light blue, passive) of cargo:NTR complexes.

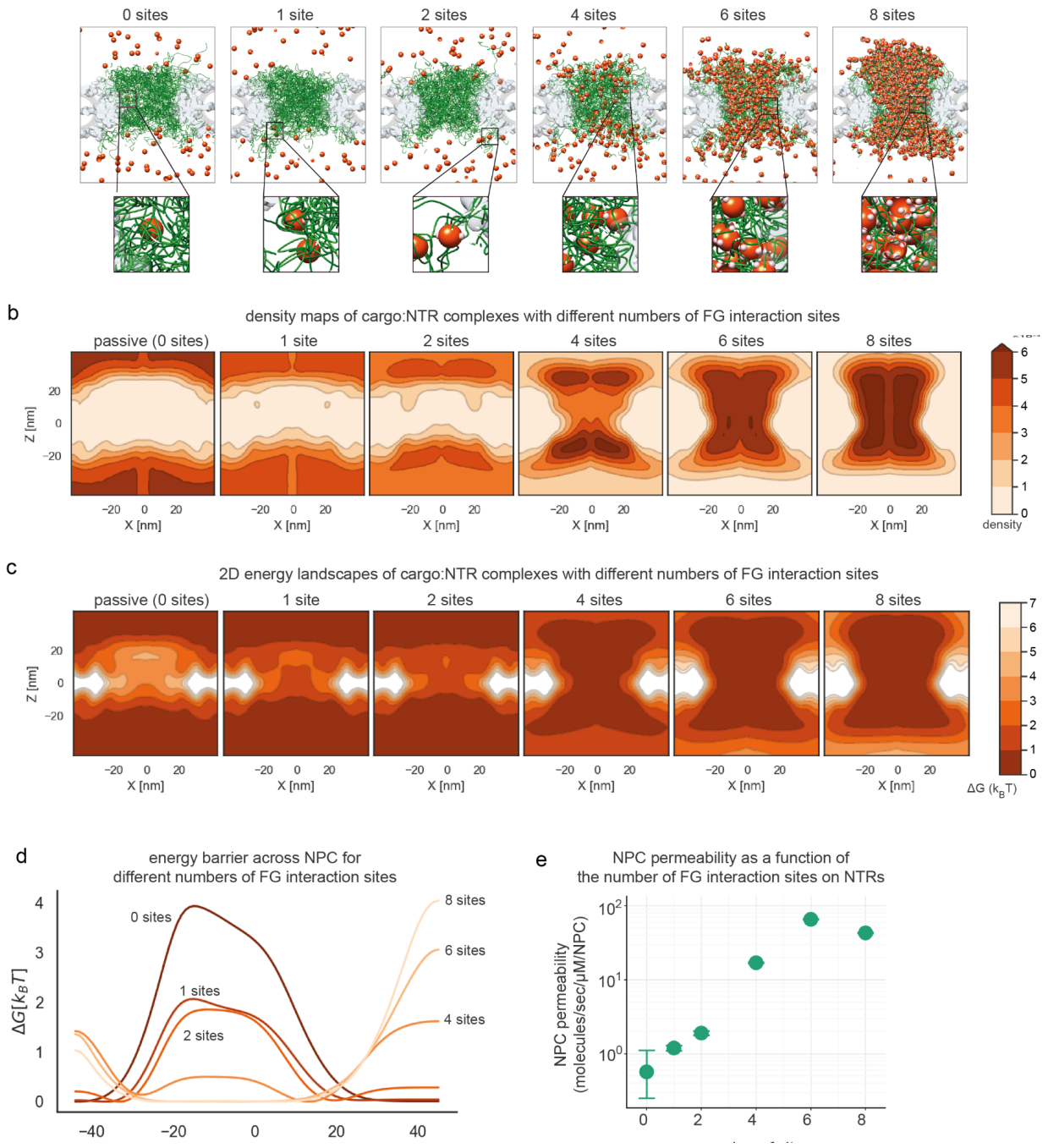

Fig. 5. Effect of NTR valency on kinetics and thermodynamics of facilitated diffusion.

a, A snapshot from a simulation showing NTR:cargo complexes (orange-red) with different NTR valencies (pink sites on NTRs) (*ie*, numbers of NTR interaction sites for FG motifs). **b**, Simulated densities for NTR:cargo complexes with different valencies. **c**, 2D Gibbs free energy landscapes (as in **Fig. 4c**) for NTR:cargo complexes with different valencies. **d**, Gibbs free energy of transport (as in **Fig. 4d**) for NTR:cargo complexes with different valencies. **e**, NPC permeability of the NPC to NTR:cargo complexes as a function of NTR valency.

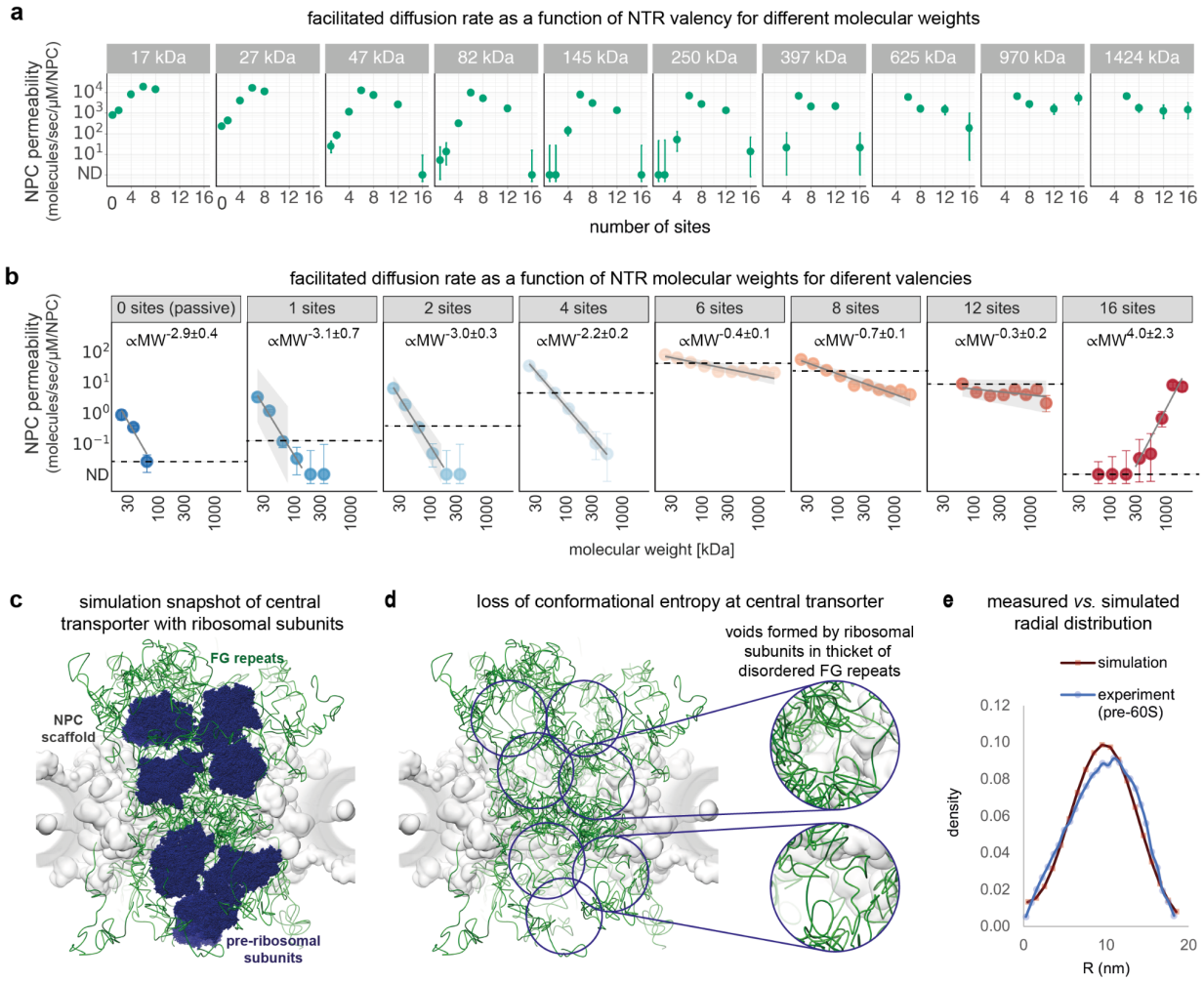

Fig. 6. Facilitated diffusion of very large cargoes with different NTR valencies.

a, NPC permeability as a function of molecular weight of the NTR:cargo complexes, shown for different numbers of FG-motif interaction sites on NTRs. ND (non-detectable) is the upper threshold of statistically reliable transport detection with 95% CI bars. **b**, Facilitated transport rate as a function of the number of FG motif interaction sites on NTRs, shown for different molecular weights of the NTR:cargo complexes. Gray line indicates fit to a power law (shaded area = 80% CI). Dashed black line indicates permeability for a 47 kDa NTR:cargo complex with specified number of interaction sites **c**, A simulation snapshot of an NPC transporting very large cargoes, equivalent in size to a late pre-40S ribosomal subunit (~1.2 MDa). All-atom representations of ribosomal subunits (PDB ID 6G18[151]) are shown at various cargo locations for illustrative purposes. **d**, Same as in **c**, without the ribosomal subunits. **e**, Simulated (red line) *vs* measured (blue line) radial distribution of similarly-sized particles at the central channel (d=15 nm simulated, d = 21 nm in experimental data on pre-60S particles[92], radial distribution in simulations computed between Z = -12 nm and Z = 12 nm along the central axis).

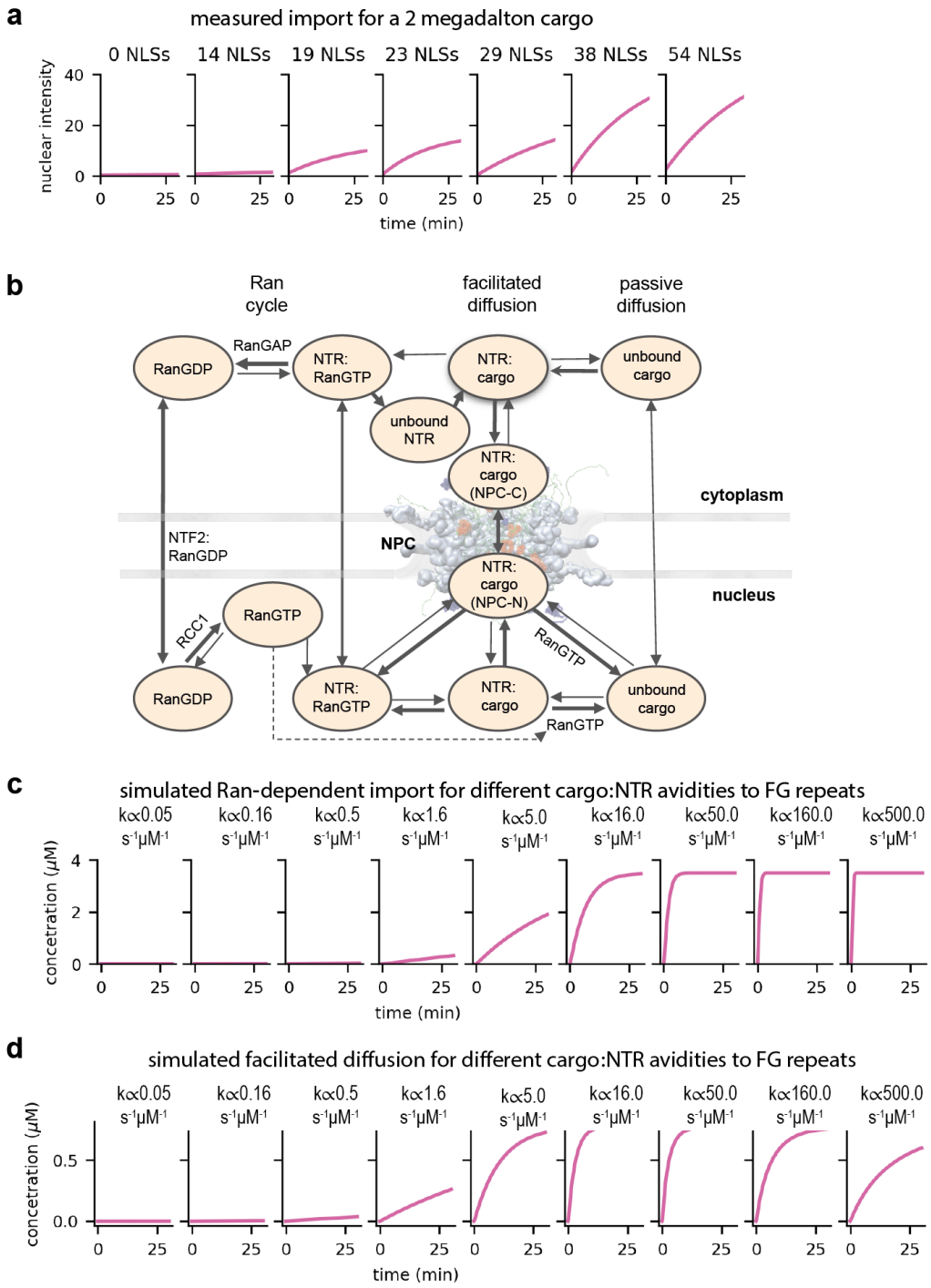

Fig. 7. Ran-dependent transport.

Experimental measurements and simulations of Ran-dependent transport and facilitated diffusion for very large cargo are compared, with the aid of a metamodel[87] that couples our previous kinetic model of transport in the whole cell[72] with the current spatiotemporal model of transport through a single NPC. **a**, Experimental measurements of Ran-dependent transport in permeabilized HeLa cells[75], showing nuclear accumulation over time for very large cargo (MS2S37P; *R*=17 nm, equivalent to a molecular weight of approximately 2 MDa), for varying numbers of nuclear localization signals (left to right). **b**, A schematic representation of the

system of ordinary differential equations describing Ran-dependent import kinetics at the whole-cell level based on a canonical description[72]. **c**, Simulations of Ran-dependent transport, showing nuclear accumulation over time for cargo of similar size, for varying magnitudes of avidity of the NTR:cargo complexes to the NPC (left to right). **d**, Same as in **c**, but for Ran-independent facilitated diffusion; here, RanGTP does not dissociate NTR:cargo complexes, which consequently dissociate at the same rate on both the nuclear and cytoplasmic sides of the NPC.

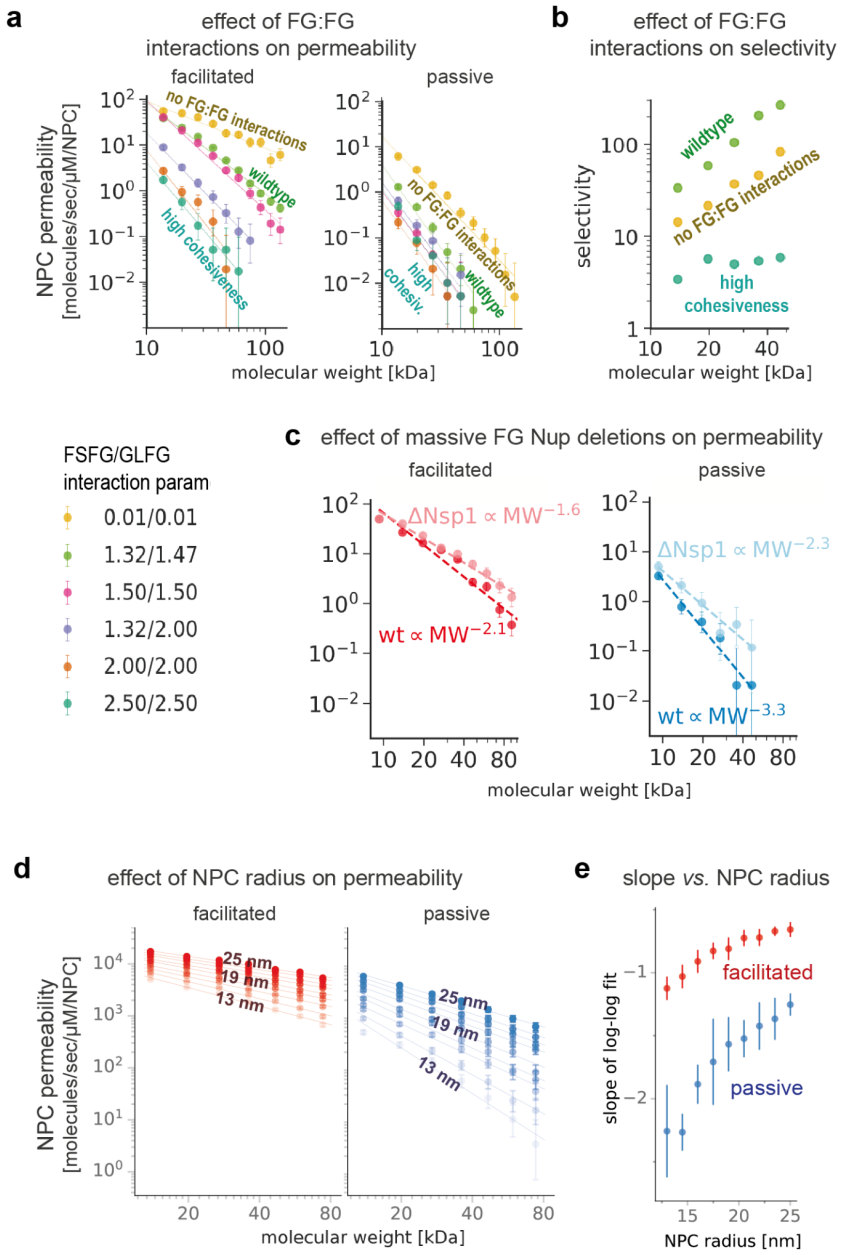

Fig. 8. Effect of NPC perturbations on its permeability.

a, NPC permeability as a function of molecular weight for different values of FG:FG interaction parameters. The color legend indicates the cohesiveness parameter for FSFG-like and GLFG-like repeats, in units of kcal/mol/A^2. **b,** NPC selectivity as a function of molecular weight for different cohesiveness levels, computed by dividing the permeability for facilitated diffusion by the permeability for passive diffusion in **a**. **c,** NPC permeability as a function of molecular weight in the model of the wildtype NPC (dark points) *vs* the ΔNsp1 deletion mutant (light points) with 95% CI, and power-law curve fits for each (dashed lines). **d,** NPC permeability as a function of molecular weight for facilitated *vs* passive diffusion for NPCs with pore radii ranging from 13 nm to 25 nm, all else being equal with 95% CI and power-law curve fits (lines), using a simplified representation of the NPC as a cylinder with 32 FG Nups. **e**, The slope of the fitted curves in **d**

as a function of the central channel radius for facilitated (red) and passive (blue) diffusion, with 95% CI.

Extended Data Figures and Tables

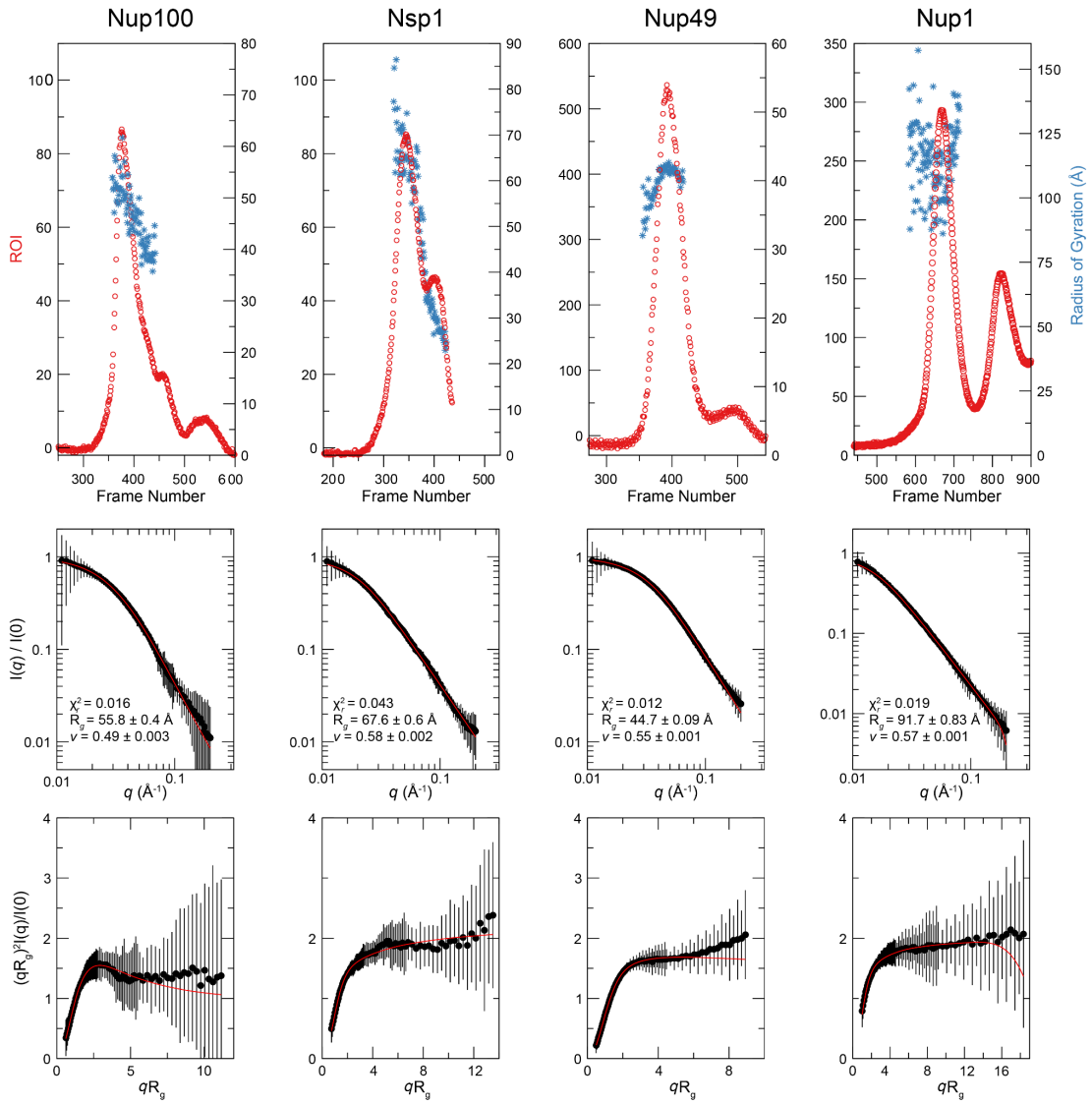

Extended Data Figure 1. Size exclusion chromatography /SAXS data for quantifying radius of gyration distributions for entire FG repeat domains.

These data were used along with data from varied sources as part of the input data during model construction (**Fig. 1b; Extended Data Table 1; Supplementary Tables 1-10**). Top row: Distribution of radius of gyration derived from the scattering in the center frames (blue) superimposed on the optical density normalized (blue) from the size exclusion runs; Center row SAXS curves of intensity *vs q* (reciprocal Å) at the peak value of above. Bottom row: Normalized (or "dimensionless") Kratky plot $(sR_g)2I(s)/I(0)$ *vs* sR_g characteristic of flexible macromolecules[152]. The horizontal or upward turning left part of each curve demonstrates a low degree of compactness from intrinsic lack of rigid structure. The sequence of each FG domain of the four FG Nups is tabulated in Supplementary Methods.

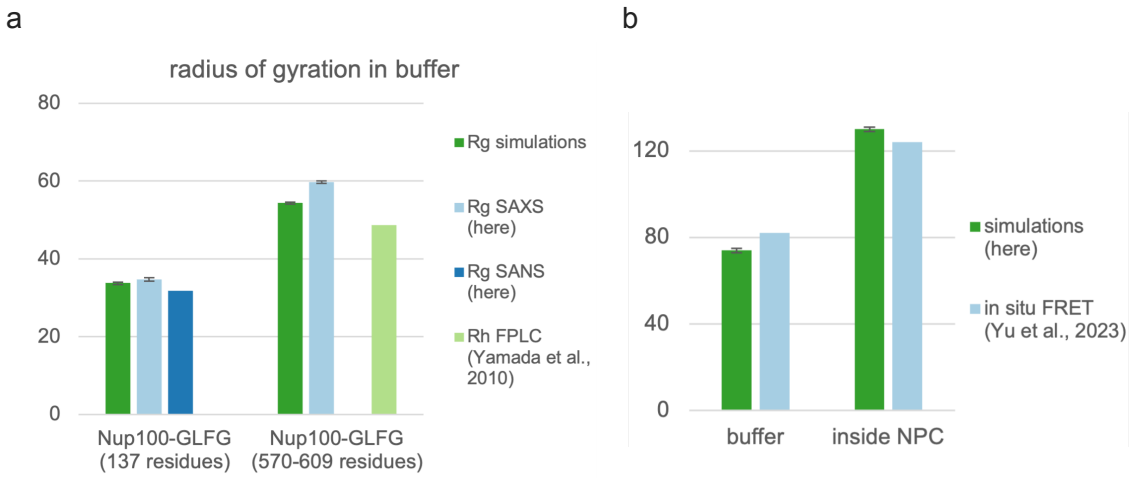

Extended Data Figure 2. Training and validation of Nup100-GLFG behavior in buffer and in the NPC.

a, Comparison of simulated and empirical training data on short *vs* long Nup100-GLFG segments in dilute buffer. In the simulations, the short and long segments of Nup100 represent 140 and 580 residues, respectively, with a single chain simulated in a bounding box of 200x200x200 nm. For the short segment, the SAXS and SANS data were collected for Nup100 residues 318-444. For the long segment, the SAXS data were collected for Nup100 residues 1-602, and the FPLC data were collected for residues 2-610 (**Supplementary Data Tables 2, 10**). **b,** Comparison of simulated and empirical validation data[74] on end-to-end distance for a 260 residues Nup100 segment between buffer and inside the NPC.

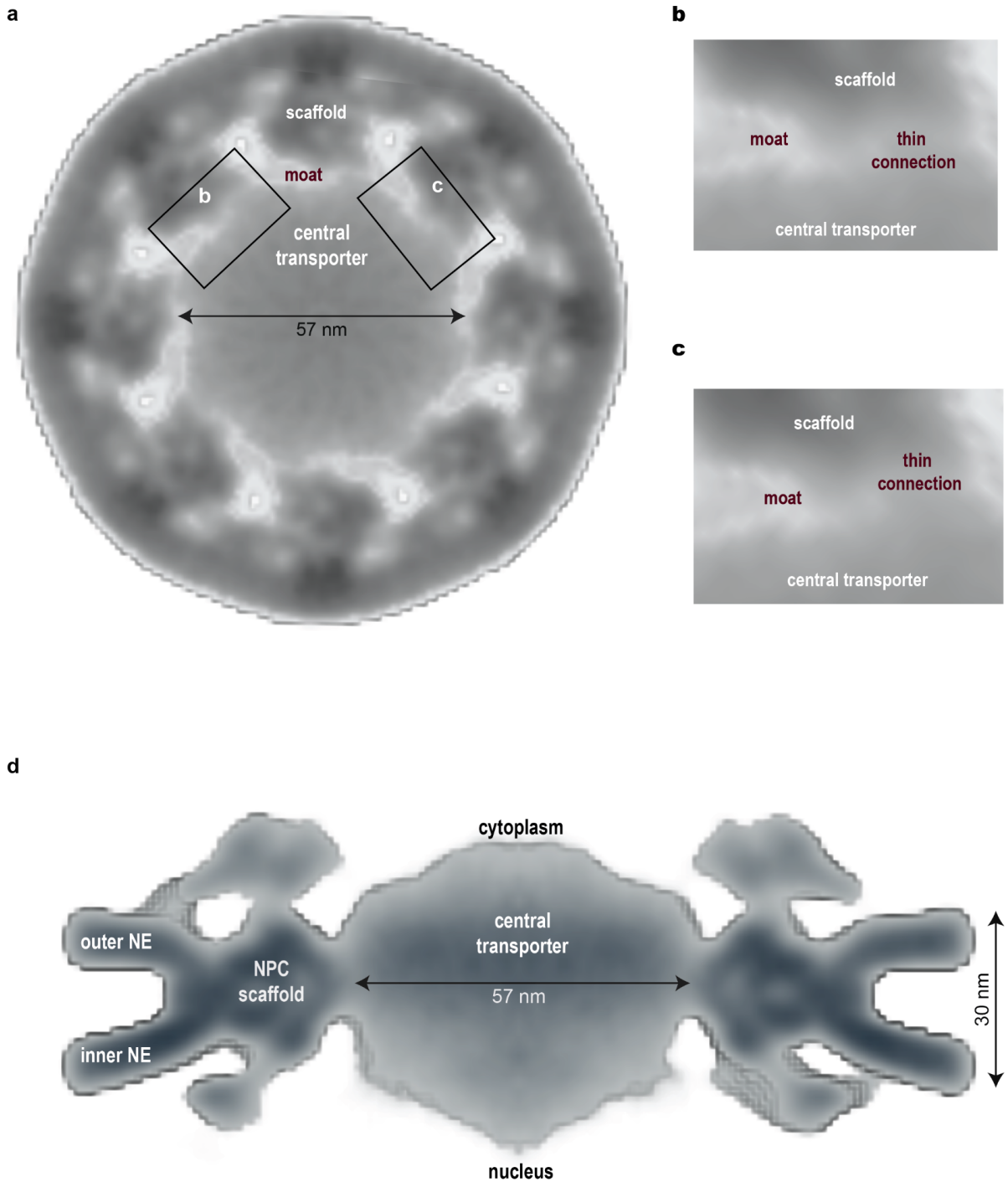

Extended Data Figure 3. *In situ* cryo-ET map of the central transporter.

a, A top view of the density at the central channel at the midpoint of the nuclear envelope from the *in situ* cryo-ET map. **b**, and **c**, Zoomed-in views of the moat region indicated in **a**. **d**, A side view of the NPC scaffold and the central transporter, embedded in the NE.

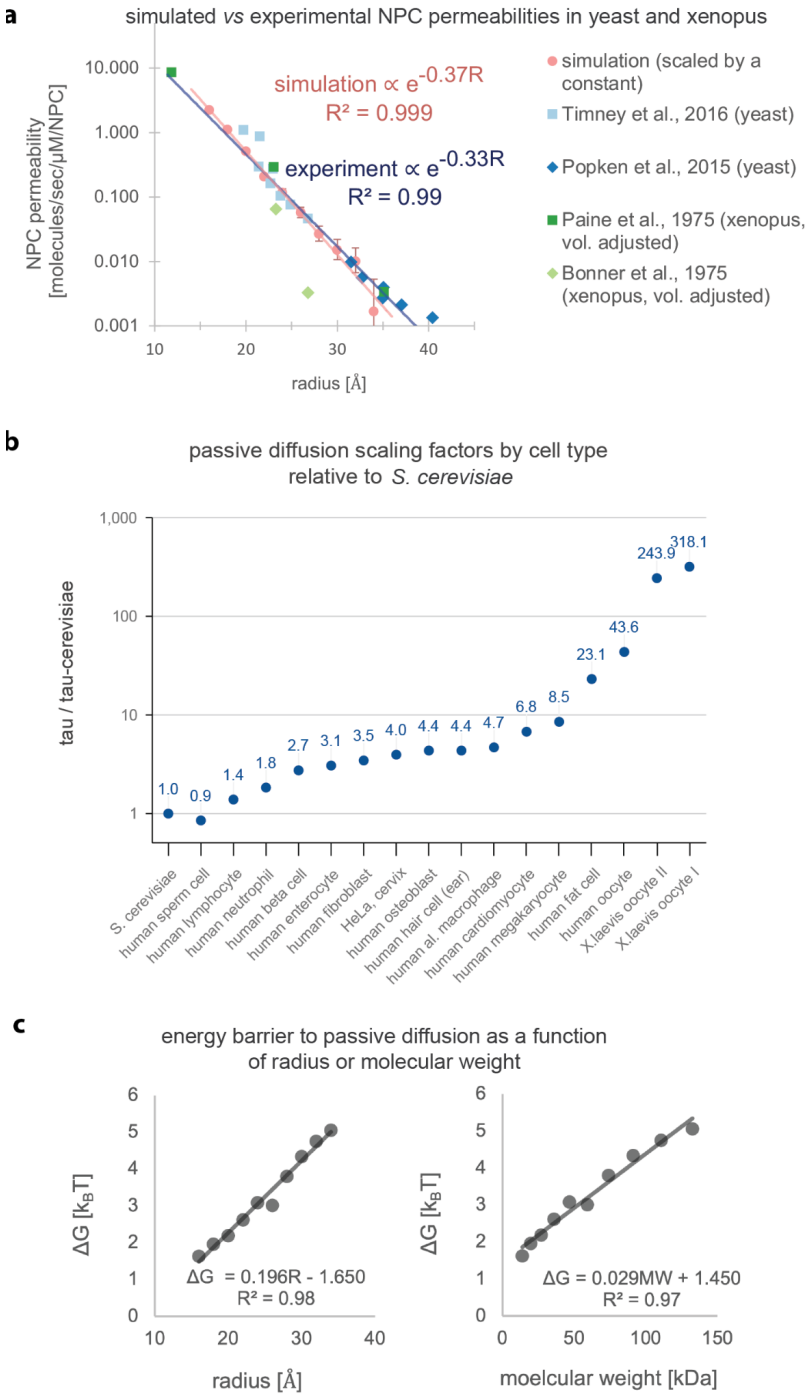

Extended Data Figure 4. Additional analyses of simulated and measured passive diffusion.

a, Comparison of simulated (pink) and experimental permeabilities from *in vivo* measurements as in **Fig. 3a**, but as a function of estimated molecular radius instead of molecular weight, shown on a log-linear scale. The pink and blue lines are exponential curves fitted to the simulated and experimental measurements in yeast, respectively. **b**, Computed scaling factors for transport time tau in various cell types compared with that for *S. cerevisiae*, based on differences in the volumes of the nuclear and cytoplasmic compartments. Transport times are

slower in larger cells due to the longer diffusion times within larger compartments, even when accounting for the larger number of NPCs. The estimates for human and *X. laevis* cells are likely to be overestimated due to the volume occupied by the many fat granules in these cell types, although they are not expected to significantly change the analysis. **c**, Gibbs free energy for passively diffusing molecules of different radii (left) or molecular weight (right).

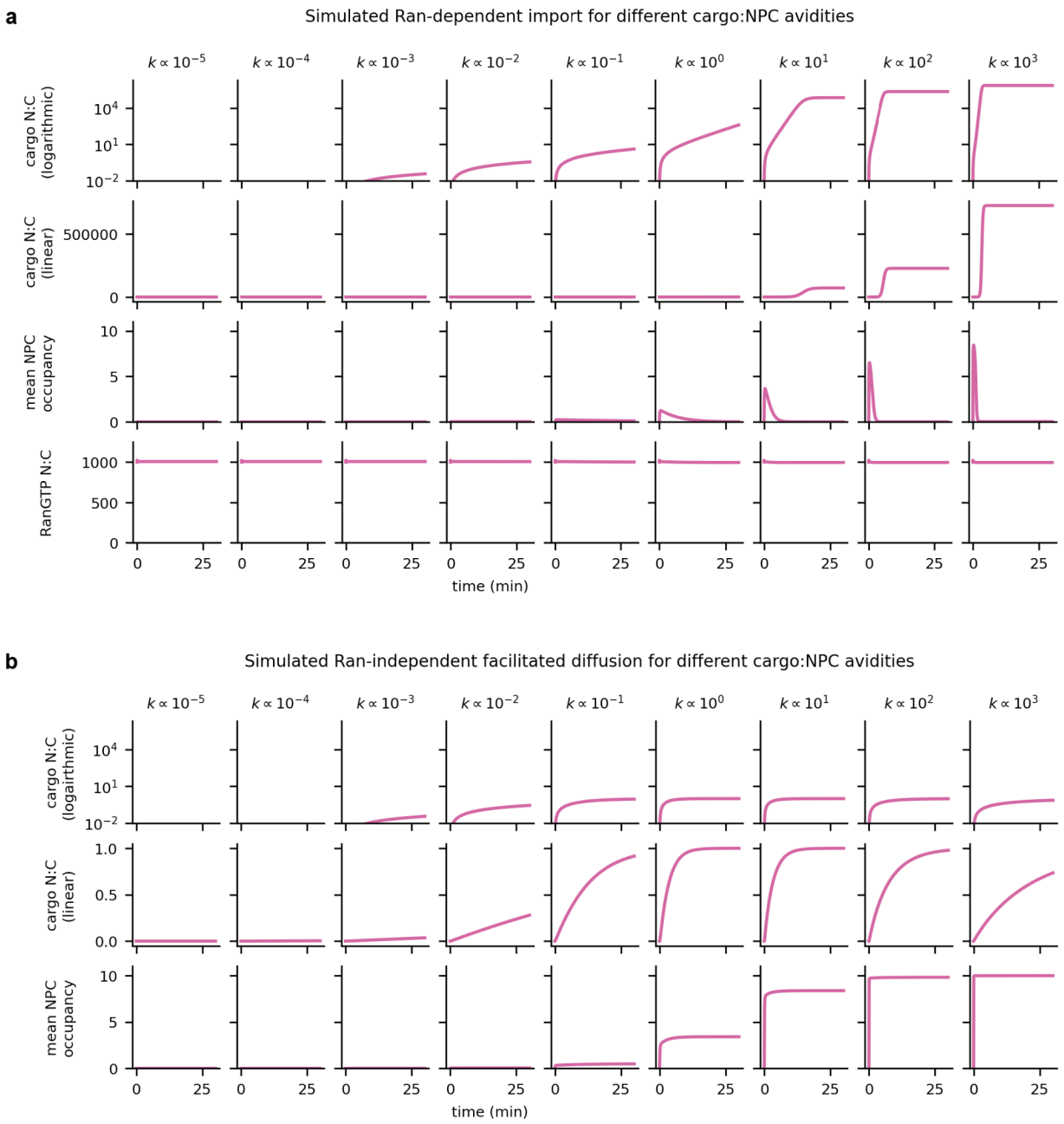

Extended Data Figure 5. Ran-dependent transport.

Simulations of transport or facilitated diffusion for very large cargo using a metamodel that couples our previous kinetic model of transport in the cell[72] with the current spatiotemporal model of transport through a single NPC. **a**, Simulations of Ran-dependent transport for varying magnitudes of avidity of the NTR:cargo complexes to the NPC (left to right), showing cargo nuclear-to-cytoplasmic ratio on a logarithmic (first row) and linear scales (second row), number of large cargo:NTR complexes occupying each NPC on average (third row); and nuclear-to-cytoplasmic ratio of RanGTP (fourth row). **b**, Same as the first three rows of (**a**) for

Ran-independent facilitated diffusion. In these simulations, RanGTP does not dissociate NTR:cargo complexes. Thus, they dissociate at the same rate on both the nuclear and cytoplasmic sides, until equilibration of the nuclear-to-cytoplasmic ratio.

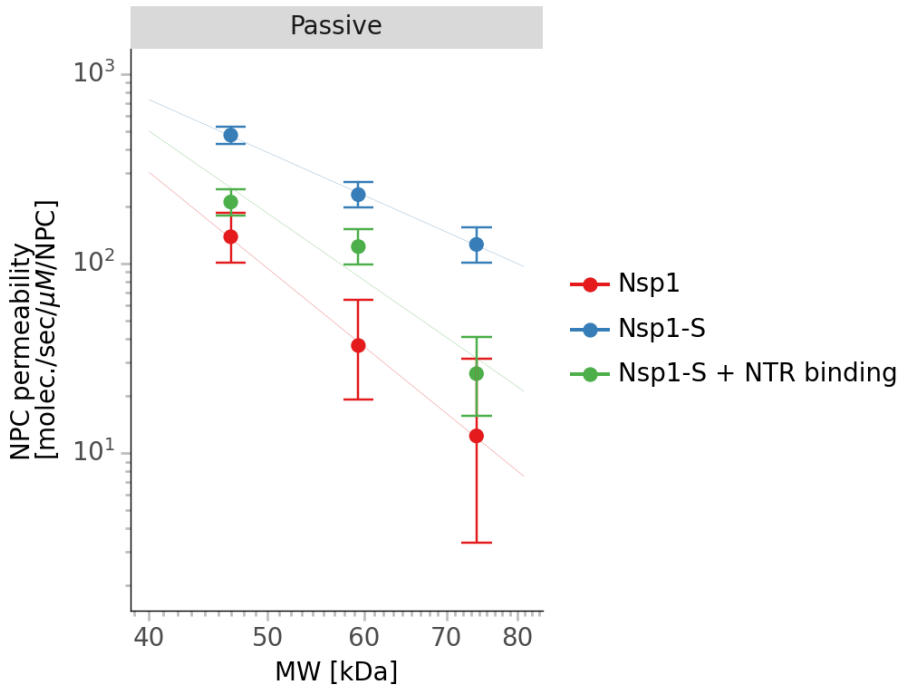

Extended Data Figure 6. Simulated passive diffusion rates in artificial nanopores as reported previously[91].

NPC permeability as a function of molecular weight for a cylindrical pore with a radius of 24 nm, lined with 104 chains of Nsp1 (red), Nsp1-S (FG mutated to SG, implying loss of both FG:FG interactions and NTR interactions; blue) or Nsp1-S with restored NTR interactions, but without FG:FG interactions (green).

Informed feature	Modeling step	Source	Reference
Nup configuration	Representation	Integrative structure model	[4]
Radius of gyration of each FG Nup	Representation Scoring Sampling	Atomistic molecular dynamics simulations	[50]
		Small angle neutron scattering (SANS)	Here, [34]
		Small angle X-ray scattering (SAXS)	Here
		Size fractionation by FPLC columns and SDS gel filtration	[39]
Radius of gyration of FG Nups upon binding	Scoring Sampling	Small angle X-ray scattering (SAXS)	Here, [34]
Persistence lengths of FG repeats	Scoring Sampling	Atomistic molecular dynamics simulations	Here
FG repeat spring constant	Scoring Sampling	Atomistic molecular dynamics simulations)	Here, [50]
FG repeat relaxation time constant	Scoring Sampling	Atomistic molecular dynamics simulations)	Here, [50]
		High-speed atomic force microscopy (hs-AFM)	[153]
Intra-FG interactions (cohesiveness)	Scoring Sampling	Full-atom molecular dynamics simulations	Here, [50]
		NMR chemical shifts (qualitatively)	Here, [47,48]
K_D (affinity), ΔH (enthalpy change), and ΔS (entropy change) of FG:NTR interactions	Scoring Filtering	Isothermal Titration Calorimetry	[90]
		NMR spectroscopy	[47,48,90]
Size-dependent passive and facilitated diffusion rates across NPC	Validation	Fluorescence recovery after photobleaching (FRAP)	[7] [78]
Transport rates of large cargo molecules	Validation	Super-resolution microscopy	[97]
		Permeabilized cell assay	[154]
Occupancy and localization of pre-ribosomal subunits	Validation	Electron microscopy, *in situ*	[155]
Density of central transporter	Representation Validation	Cryo-electron tomography of isolated NPC, *in vitro*	[4]
	Validation	Cryo-electron tomography, *in situ*	Here
Dynamics of central transporter	Validation	Atomic Force Microscopy	[93]
		FRET	[74]

Extended Data Table 1. Input information for modeling.

See Supplementary Methods for details.

FG Nup	GLFG-like residues	FSFG-like residues	Non-FG (disordered) residues	Anchor residue(s)	Copy number	FGs/Nup
Nsp1	1-180	181-550	551-636	637-637	48	36
Nup100	1-550		551-800	801-815	16	48
Nup116	1-750		751-950	951-965	16	53
Nup159		442-881*	882-1116	1117-1117	16	30
Nup49	1-240		241-269	270-270	32	17
Nup57	1-200		201-286	287-287	32	15
Nup145	1-200		201-250	251-275	16	15
Nup1	816-1076	326-815	201-325	151-200	8	36
Nup2		183-562	563-582	583-720**	16	23
Nup60		399-539	301-398	251-300	16	8
Nup42	Omitted, due to uncertainty regarding its anchor point as well as relatively small size and copy number.					

* non-specific k modified to 0.07 kcal/mol/Å for Nup159 FSFG-like residues

** Nup2 did not appear in the integrative model of the NPC [4]; the same anchor as for Nup60 is used instead based on information about Nup60:Nup2 interaction[156]

Extended Data Table 2. FG repeat domains of FG Nups, their flavors, and anchor points.

Supplementary videos

Supplementary Video 1

https://drive.google.com/open?id=12qSS4Y0xKijj49tyHayOE1JWG29AAXvL&usp=drive_fs

A sample Brownian Dynamics simulation trajectory from our model of transport through the nuclear pore complex. The scaffold of the NPC is shown in yellow surface representation. FG repeat domains of different FG Nups are anchored to the scaffold (tube representation in various hues). Inert (passively-diffusing) macromolecules that do not interact with the FG repeats are represented as blue spheres of different radii, corresponding to different molecular weights. Note the size dependency of passive diffusion. Cargo:NTR complexes that interact with the FG repeats are represented as red spheres of different radii, also corresponding to different molecular weights.

Supplementary Video 2

https://drive.google.com/file/d/1FzVrpmqUOA2kWnNZ1PZlEUuJHF5dAUgP/view?usp=sharing

A 12 μs Anton2 simulation of the interaction between Kap95 (gray cartoon representation) in the presence of the Nsp1-derived FSFG6 construct[50] with six consecutive repeats of FSFG repeats (pink representation; phenylalanine residues in pink space-fill representation). The surface representation on Kap95 indicates cumulative contact areas, colored by the fraction of time in contact with FSFG motifs of FSFG6 up until the current point in the simulation, from ~0% in blue (short transient contacts, *eg,* probing a local surface non-specifically) to 100% in red (longer-lived contacts in grooves in between external helices).

Supplementary Video 3

https://drive.google.com/open?id=12zDlvzgAVmDr773OPKcjYAwVdVN2tZG4&usp=drive_fs

Sliding of an FSFG motif (residues 88-91 of FSFG6) about its interaction site with Kap95, as visualized by tracking its center of mass over a 1.5 μs simulation on Anton2. The simulation itself included two FSFG6 constructs, but only a single FSFG motif from the first chain is shown for clarity. The arrows indicate the principal components computed by applying principal component analysis to the set of FSFG center of mass coordinates, similarly to a similar computation for FSFG:NTF2 interactions in Raveh et al., 2016, Figure 4[50]

Supplementary Methods

Representation of model components, interactions, and dynamics

The model of nucleocytoplasmic transport was implemented in our open source *Integrative Modeling Platform* (IMP) software (http://integrativemodeling.org)[35,83,85] using a previously published protocol for Brownian dynamics simulations [4,7]. The input files, scripts, and output files for the simulations are deposited in a GitHub repository that will be made publicly available along with the final version of this manuscript.

Model components

The simulated components include the static ring-shaped scaffold of the NPC, the NE, disordered and flexible FG repeat domains of FG Nups, NTR:cargo complexes, and passively diffusing macromolecules, all enclosed within a bounding box of 200 x 200 x 200 nm. The configuration of these components is fully specified by a configuration vector X that includes their spatial coordinates, their orientation vectors, and the values of some auxiliary variables, as detailed in Section "Interactions among model components".

The integrative model of the NPC scaffold [4] was coarse-grained to increase the computational efficiency of the simulations while maintaining a relatively high accuracy of representation near FG Nup anchor points: the static scaffold surface was approximated by a collection of spherical particles using the IMP `get_simplified_from_volume()` method, with an approximation error of $min(0.3x(max(2.0, d) - 1)^{1.2}, 5.0)$ nm between the surface of the original representation and the surface of the new coarse-grained representation, where d is the minimal distance between the center of an approximated sphere and any FG Nup anchor point; this approximation implies a deviation from the original NPC scaffold of less than 0.3 nm near the anchor residues of the FG repeats. The NE was represented as a 30 nm slab (based for example on the *in situ* cryo-ET map in **Extended Data Fig. 3**) with a toroid pore (outer radius R = 5.4 nm; inner radius r = 39 nm). The disordered domain of each FG Nup (FG repeat domain), typically consisting of 8-53 FG repeats and 250-1000 residues (**Extended Data Table 2**), was represented as a flexible string of beads (spherical particles), each one of which has a radius of 8 Å and encompasses 20 residues (**Extended Data Table 2**) [4,7], except for Nup42 that was omitted from the model because of the uncertainty regarding its anchor point as well as a relatively small size and copy number. An FG repeat domain was divided into either GLFG-like, FSFG-like, or non-FG segments, and anchored to the C-terminus of its globular anchor domain (**Extended Data Table 2**). The number of beads was calculated for each segment separately and rounded up. The FG repeat domain of Nup2, which was not included in the original integrative structure of the NPC [4], was anchored to the same anchor domain as Nup60 based on the known interaction between the two anchor domains [156,157]. Each bead also has a single specific interaction site on its surface, representing an FG motif that may interact with other FG motifs and with NTRs.

Each NTR:cargo complex was represented as a single spherical particle of radius r with n specific interaction sites, randomly distributed on its surface. Each passively diffusing molecule was modeled as a single spherical particle of radius r. To plot the results of simulations (which only depend on r) as a function of molecular weight, we assumed that each sphere has a uniform protein density of 1.38 g/cm^3 [158], resulting in $MW = \frac{4}{3}\pi r^3 \rho$ kDa. Alternatively, the radius can be interpreted as the Stokes radius of the molecule,, resulting in $MW = (r/6.6)^3$ kDa [159], leading to nearly identical values for the molecular weight.

Interactions among model components

Interactions among the model components were quantified using a coarse-grained potential energy function $U(X)$, where X is the configuration vector:

$$U(X) = U_{\text{excluded}} + U_{\text{FG-polymer}} + U_{\text{FG-cohesiveness}} + U_{\text{FG:NTR}} + U_{\text{non-specific}} \text{ kcal/mol}$$

where X was omitted on the right side of the equation for simplicity. We now explain each one of these terms in turn.

I. Excluded volume term

$$U_{\text{excluded}} = -\, k_{\text{ex}} \cdot \left(\sum_{\{i,j|\hat{d}_{i,j}<0\}} \hat{d}_{i,j} + \sum_{\{i|\hat{d}_{i,NE}<0\}} \hat{d}_{i,NE} + \sum_{\{i|\hat{d}_{i,BB}<0\}} \hat{d}_{i,BB} \right) \text{kcal/mol}$$

U_{excluded} is a linear excluded-volume potential that penalizes overlaps between model components. $\hat{d}_{i,j}$ denotes the minimal distance between the surfaces of the ith and j^{th} particles; with radii r_i and r_j, respectively; it is equal to $d_{i,j} - r_i - r_j$, taking a negative value when the two particles intersect and zero when they touch externally. Similarly, $\hat{d}_{i,BB}$ denotes the minimal distance between the surface of the ith particle and the simulation bounding box. $\hat{d}_{i,NE}$ denotes the minimal distance between the surface of the ith particle and the NE. k_{ex} is a force constant of 10 kcal/mol/Å, allowing a soft overlap of 1-2 Å between the coarse-grained representations of the model components.

II. FG polymer term

$$U_{\text{FG-bond}} = \sum_{FG \in FGs} \sum_{i=0}^{n_{FG}-1} 0.5 \left[k_{b1} \left(d_{i,i+1} - d'_{i,i+1} \right)^2 + k_{b2} \left(d'_{i,i+1} - d'^{rest}_{i,i+1} \right)^2 \right] \text{kcal/mol}$$

$U_{\text{FG-bond}}$ is a harmonic bonded interaction potential accounting for the spring-like nature of flexible polymers in general [105] and disordered FG repeat domains in particular [30,37,47,48,50,153,160]. $d_{i,i+1}$ denotes the distance between the centers of the ith and $(i+1)^{\text{th}}$ beads in a single FG repeat domain $FG \in FGs$ that has n_{FG} beads. For each pair of consecutive beads, the potential includes the sum of two harmonic terms. The first term couples $d_{i,i+1}$ to $d'_{i,i+1}$, a slow-diffusing auxiliary

variable representing the momentary rest distance. The second term couples $d'_{i,i+1}$ to $d'^{rest}_{i,i+1}$, the equilibrium rest length between consecutive repeats. The indirect coupling of $d_{i,i+1}$ to $d'^{rest}_{i,i+1}$ *via* $d'_{i,i+1}$ was used to include information about the empirical relaxation time for the end-to-end-distance between consecutive repeats, analogously to the coupling of fast-moving variables to auxiliary slow-moving variables in temperature-accelerated molecular dynamics simulations [161,162]. The value of $d'^{rest}_{i,i+1}$ was typically set to 30.4 Å[50] but it can fluctuate due to changes to the model parameters when fitting to the data. This value is an input to the simulations; it may differ from the output (apparent) resting distance emerging out of the simulations due to, for example, cohesive interactions within or between FG repeats or the constricted volume within the central channel, all of which may act to either increase or decrease the output resting distance. The value of the first coupling coefficient k_{b1} was set to guarantee a small standard deviation σ_1 = 2.0 Å of the difference between $d_{i,i+1}$ and $d'_{i,i+1}$. The value of k_{b1} was computed by equating the normal and Boltzmann distributions of the spring length, $e^{-0.5(d_{i,i+1}-\hat{d}_{i,i+1})^2/\sigma^2} = e^{-0.5k_{b1}(d_{i,i+1}-\hat{d}_{i,i+1})^2/k_BT}$, where k_BT is the Boltzmann constant 0.0019872041 kcal/mol/K [163]) and T is the simulation temperature. From this equality, we inferred that $k_{b1} = k_BT \cdot \sigma_1^{-2}$ $\sigma_1 = \sqrt{k_BT \cdot k_{b1}^{-1}}$. Distance-dependent contributions to configurational entropy to the right hand term can be neglected because $d_{i,i+1} - d'_{i,i+1} << d_{i,i+1}$. Similarly, the value of the second coupling coefficient k_{b2} was typically set to 0.0075 kcal/mol/Å^2 implying a standard deviation of $\sqrt{k_BT \cdot k_2^{-1}}$ = 8.9 Å for the distance between two consecutive beads in the FG repeat domains. The diffusion coefficient $D_{i,i+1}$ of the auxiliary variable $\hat{d}_{i,i+1}$ was set to $k_BT \cdot \tau^{-1} \cdot k_{b2}^{-1}$ Å^2/fs, where τ is the estimated relaxation time of the distance between two consecutive FG repeats; it was typically set to 50 ns (50x10^6 fs) for all FG repeats unless stated otherwise (**Extended Data Table 1)**. This computation is based on the relaxation time of a polymer chain being equal to $\zeta \cdot k_{b2}^{-1}$ [105], where ζ is the hydrodynamic friction coefficient of the Brownian dynamics, which is equal to $k_bT \cdot D_{i,i+1}^{-1}$ (see Dynamics of the model below).

III. FG cohesiveness term

$$U_{\text{FG-cohesiveness}} = \sum_{i,j} L(d_{i_0 j_0}) \quad \text{kcal/mol}$$

$U_{\text{FG-cohesiveness}}$ is an isotropic non-bonded linear interaction potential representing cohesive interactions between pairs of interaction sites on FG repeats. $L(d_{i_0 j_0})$ is a truncated linear

restraint on $d_{i_0 j_0}$, the distance between the interaction sites on the ith and j^{th} FG beads, respectively. It is equal to $0.5(k_{\Psi_i} + k_{\psi_j})d_{i_0,j_0}$ when $d_{i_0,j_0} < 0.5(R_{\psi_i} + R_{\psi_j})$ or zero otherwise, where ψ_i and ψ_j are the flavors of the ith and j^{th} FG beads, respectively; k_{ψ_i} and k_{ψ_j} are the force coefficient for the corresponding flavors, parameterized as follows: $k_{GLFG-like} = 1.55$ kcal/mol/Å; $k_{FSFG-like} = 1.50$ kcal/mol/Å; $k_{disordered} = 1.50$ kcal/mol/Å; and R_{ψ_i} and R_{ψ_j} are the maximal range for cohesive interaction of FG repeats for the corresponding flavors, parametrized to 6 Å for all FG flavors.

IV. FG:NTR interaction term

$$U_{\text{FG:NTR}} = 0.5k_{NTR} \cdot \sum_{i_m,j_n} \varphi_{i_m,j_n} H(\hat{d}_{i,j}) \text{ kcal/mol}$$

$U_{\text{FG:NTR}}$ is an anisotropic non-bonded interaction potential between interaction sites on NTRs and FG repeat domains, that takes into account both the distance between the FG repeats and the NTR:cargo complex, and the relative orientation of their interaction sites with respect to one another. The anisotropy is intended to reflect the observed sliding of FG motifs on the surface of NTRs in full-atom molecular dynamics simulations that reproduce experimental R1/R2 relaxation data from NMR and are consistent with the elongated chemical shifts signal on FG interaction sites on NTRs [50]. k_{NTR} is the force coefficient for this interaction term, and it was set to 5.98 kcal/mol/Å^2 in all simulations unless stated otherwise. φ_{i_m,j_n} is a unitless anisotropic attenuation factor that is equal to 1.0 when the interaction sites of the mth interaction site on the ith NTR:cargo complex and the nth interaction site on the jth FG bead are facing each other and 0.0 when they are rotated beyond a certain angle; formally, it is equal to $max(0, \frac{cos(\Theta_{i_m,j}) - cos[max\Theta_1)]}{1 - cos[max\Theta_1]}) \cdot max(0, \frac{cos(\Theta_{2,i_m,j_n}) - cos[max\Theta_2]}{1 - cos[max\Theta_2]})$, where $\Theta_{i_m,j}$ is the angle formed between the mth interaction site of the ith NTR:cargo complex, the center of the ith NTR:cargo complex, and the center of the jth FG bead; and Θ_{i,j_n} is the angle formed between the center of the ith NTR:cargo complex, the center of the jth FG bead, and the nth interaction site, and the jth FG bead. $\max\Theta_1$ and $\max\Theta_2$ were both set to $\frac{\Pi}{4}$. $H(\hat{d}_{i,j})$ is a truncated harmonic restraint on $\hat{d}_{i,j}$, the minimal distance between the surfaces of the NTR:cargo complex and the FG bead. It has a maximal range of R_{NTR}. When $\hat{d}_{i,j}$ is lower than $\frac{1}{2}R_{NTR}$, it is equal to $\hat{d}_{i,j}^{\ 2} - \frac{1}{2}R_{NTR}^{\ 2}$; and in the range $0.5R_{NTR} < \hat{d}_{i,j} < R_{NTR}$, it is equal to $(R_{NTR} - \hat{d}_{i,j})^2$. R_{NTR} was set to 5.5 Å unless specified otherwise.

V. Non-specific interaction term

$$U_{\text{non-specific}} = \sum_{i \in FGs, j} L(\hat{d}_{i,j}) \text{ kcal/mol}$$

$U_{\text{non-specific}}$ is an isotropic non-bonded linear interaction potential representing non-specific interactions between FG repeats and any diffusing molecule in the simulations, i.e. NTR:cargo complexes, passively diffusing molecules and other FG repeats. $L(\hat{d}_{i,j})$ is a truncated linear restraint on $d_{i,j}$, the minimal distance between the surfaces of the ith FG bead and the jth diffusing particle in the simulation. It has a maximal range of R_{ns}. If the second particle is an FG bead, it is equal to $\sqrt{k_{ns[\Psi_i]} k_{ns[\psi_j]}} d_{i,j}$ when $d_{i,j} < R_{ns}$ or zero otherwise, where $k_{ns[\psi_i]}$ and $k_{ns[\psi_j]}$ are the non-specific force coefficients for flavors ψ_i and ψ_j of the corresponding beads; if the second particle is not FG bead, it is equal to $k_{ns[\Psi_i]} d_{i,j}$ when $d_{i,j} < R_{ns}$ or zero otherwise, where $k_{ns[\psi_i]}$ is the non-specific force coefficients for flavors ψ_i. Unless stated otherwise, $k_{ns[FSFG-like]}$ was set to 0.01 kcal/Å, $k_{ns[GLFG-like]}$ was set to 0.08 kcal/mol/Å, $k_{ns[Nup159]}$ was set to 0.07 kcal/mol/Å, and $k_{ns[disordered]}$ was set to 0.01 kcal/mol/Å. R_{ns} was set to 5.0 Å for all FG flavors.

Dynamics of the model

Brownian dynamics simulations [94] were implemented in IMP as described previously [4,7]. All simulations were conducted at 297.15 K. The force vector $\vec{f}(X_i)$ is acting on the ith particle with coordinates X_i. It is equal in magnitude and opposite in direction to the gradient $\nabla U(X_i)$. The coordinates of all non-static particles (FG repeat domains, NTR:cargo complexes, and passively diffusing molecules) were updated at each time step using the following discrete integration equation:

$$X_i(t + \Delta t) = X_i(t) + \frac{D}{k_B T} \Delta t \vec{f}(X_i) + \sqrt{2D\Delta t} R$$

where t denotes time, Δt is the integration time step, D is a translational diffusion coefficient assigned to each bead in units of Å^2/fs, $k_B T$ is as described above, and R is a standard normal random variable with the mean of 0 and the standard deviation of 1. The term $\frac{D}{k_B T}$ is denoted ζ, the hydrodynamic friction coefficient for the diffusing particles. Torques between interaction sites on FG repeats and NTR:cargo complexes were integrated similarly to the integration of translational forces, but using a rotational diffusion coefficient D_{rot} instead of D, specified in units of rad^2/fs. The sum of the torques was multiplied by $\frac{1}{k_B T} D_{rot} \Delta t$, followed by adding it to a random rotation about a uniformly sampled rotation axis; the magnitude of the rotation is a

normal random variable with mean 0 and standard deviation of $\sqrt{6D_{rot}\Delta t}$, approximating an independent rotation around three rotational degrees of freedom of magnitude $\sqrt{2D_{rot}\Delta t}$ each.

To approximate the differences between diffusion rates of molecules of different sizes, we defined the Stokes radius of each bead to equal its radius r. We then assigned each bead a translational diffusion coefficient in units of Å^2/fs using the Stokes-Einstein equation, $D = \frac{k_B T}{6\pi\eta r}$, where η=0.92 mPa·s is the dynamic viscosity of water at 297.15 K. Each bead was also assigned a random rotational diffusion coefficient $D_{rot} = \frac{k_B t}{8\pi\eta r^3}$, in units of rad^2/fs, using the Einstein-Stokes-Debye equation, and multiplying η by a constant factor of 3.33 to account for increased viscosity in the crowded molecular environment[164].

In situ cryo-electron tomography of *S. cerevisiae* NPC

Saccharomyces cerevisiae W303 cells, collected during their logarithmic growth phase, were deposited onto electron microscopy grids and rapidly vitrified by plunge-freezing into liquid ethane-propane mixture. In cryogenic conditions, lamellae were generated from the clusters of yeast cells using cryogenic-focused ion beam (cryo-FIB) milling in an Aquilos Dual-Beam system (Thermo Fisher Scientific). More specific details of the cryo-FIB milling have been described previously[165]. The tilt-series data was collected on a Titan Krios G3 electron microscope (Thermo Fisher Scientific) operated at 300 kV, with a post-column energy filter and K2 Summit direct detector (Gatan) in counting and dose fractionation modes. Parameters for the tilt-series were: Tilt range of ± 45-60°, pixel size of 3.45 Å, tilt increments of 3° (4-5° for some), and a defocus range of -2 to -11 µm. SerialEM was used for data collection[166]. Additional data from EMPIAR-10466 was integrated into the dataset.

Tilt-series processing and alignment

The tilt image frames underwent motion correction via WARP[167], applying a motion model of grid 3 by 3. The corrected frames were then collated into tilt-series stacks within WARP. These motion-corrected series were subsequently aligned using AreTomo[168]. Post alignment, the stacks were reintegrated into WARP for CTF estimation, determination of defocus handedness, and final reconstruction. All tilt series' CTF estimations and defocus handedness were manually checked and adjusted if necessary.

Generation of subtomograms containing NPCs

From the aligned tilt-series, tomograms were reconstructed in WARP[167]. The NPC particles in these tomograms were manually picked and assigned initial orientations normal to the nuclear membrane. The subtomograms of the individual NPC particles, totaling to ~4000, were generated in WARP at pixel size of 10 Å.

Model creation, refinements, and classification

A select group of NPC particles were used to generate an initial C_8 symmetrized model. This initial model was used for initial refinement, with C_8 symmetry, using localized searches around the initial orientation (*ie*, initial Euler angles). After the refinements, bad particles were removed using 3D classification and manual inspection. The good particles underwent further refinement with the C_8 symmetry to generate the final *in situ* map. All these steps were performed in Relion3[169].

Additional Supplementary Material

Additional supplementary material including additional supplementary tables for this manuscript can be found in the following link:

https://docs.google.com/document/d/1pyDS-FGiYeUFrGMy4x7YMr96gezvcS0XQMlTLkf6AVg/edit?usp=sharing